Construction and Building Materials 355 (2022) 129128

Contents lists available at ScienceDirect

Construction and Building Materials

journal homepage: www.elsevier.com/locate/conbuildmat

Cementation processes of Roman pozzolanic binders from Caesarea Maritima (Israel)

Michele Secco [a,b,*], Yotam Asscher [c], Giulia Ricci [b,d], Sergio Tamburini [e], Nereo Preto [d], Jacob Sharvit [c], Gilberto Artioli [b,d]

[a] University of Padova, Department of Cultural Heritage (DBC), Italy
[b] University of Padova, Inter-Departmental Research Center for the Study of Cement Materials and Hydraulic Binders (CIRCe), Italy
[c] Israel Antiquities Authority (IAA), Israel
[d] University of Padova, Department of Geosciences, Italy
[e] National Research Council, Institute of Condensed Matter Chemistry and Technologies for Energy (CNR-ICMATE), Italy

ARTICLE INFO

Keywords:
Pozzolanic reaction
Opus caementicium
Harbor engineering
Caesarea Maritima
Phlegraean Fields
Calcium-aluminosilicate-hydrate (C–A–S–H)
Magnesium-silicate-hydrate (M–S–H)
Sulphate-reducing-bacteria (SRB)
Rietveld quantitative phase analysis
Nuclear magnetic resonance (NMR)

ABSTRACT

A multi-analytical characterization study was performed on the pozzolanic binding composites used for the construction of Sebastos harbor in Caesarea Maritima, comparing underwater concretes to on-land mortars. Historically dated to the 1st Century BCE, the structure was erected by King Herod the Great as the largest ancient artificial harbor in the open sea. The combined interpretation of the results obtained through petrographic, mineralogical, spectroscopic, and microstructural/microchemical analyses indicated the use of different binder recipes, related to Roman and Phoenician-Punic technological practices, employing both natural volcanic pozzolans and artificial pozzolanic additives derived from the combustion of organics. Furthermore, the study unraveled the complex cementation processes of the binding composites, influenced by diversified chemical-physical-biological conditions of the precipitating environment such as water salinity and bacterial activity, leading to the formation of unconventional carbonates, as well as peculiar hydrated calcium aluminosilicate (C–A–S–H) and magnesium aluminosilicate (M–A–S–H) phases. The results constitute a relevant contribution to the understanding of the reactive pathways of ancient and modern pozzolanic systems.

1. Introduction

The discovery of pozzolanic reaction through the employment of pozzolanic additions, amorphous aluminosilicate compounds reacting with lime and water and precipitating nanostructurally-polymerized insoluble phases with excellent mechanical, permeability and durability properties [1], constituted the most relevant technological evolution in the field of inorganic binders since the beginning of pyrotechnology. The broad term "pozzolanic reaction" gathers all the chemical processes leading to the dissolution and recombination of alumino-silicate materials and calcium hydroxide in a highly alkaline lime-saturated aqueous solution to form hydrated reaction products (calcium silicate and calcium aluminate hydrates) with marked binding properties related to their nanostructured crystal habits, according to the following simplified reaction expressed in cement chemistry notation ($A = Al_2O_3$; $C = CaO$; $H = H_2O$; $S = SiO_2$):

$$AS + CH + H \rightarrow C\text{–}S\text{–}H + C\text{–}A\text{–}H$$

A plethora of pozzolanic materials was employed since ancient times as additions in hydraulic lime mortars, namely natural or synthetic silica glasses, volcanic ashes, diatomaceous earths, phytoliths, ceramics, clays, ashes from burnt organics and metallurgical slags [2], with several of these still used in modern binders as supplementary cementitious materials (SCM) [3,4].

After sporadic and probably involuntary applications dating back to the Neolithic period [5], the employment of pozzolanic materials in lime-based binders saw a significant diffusion in the Greek and Aegean world during the 2nd millennium BCE, with diffuse technological transfers in the following centuries in the Mediterranean basin, such as among the Phoenician-Punic and Etruscans [2,6]. Construction practices using pozzolanic mortars, mainly *cocciopesto* obtained by mixing lime with finely ground brick powders [7], were still limited by those times to the production of waterproof floors and cistern plasters, with no attested structural applications [2]. Nevertheless, such early experimentations

* Corresponding author.
E-mail address: michele.secco@unipd.it (M. Secco).

https://doi.org/10.1016/j.conbuildmat.2022.129128
Received 11 April 2022; Received in revised form 7 September 2022; Accepted 8 September 2022
Available online 2 October 2022

constituted the technological background adopted by Ancient Romans for the formulation of their groundbreaking proto-concrete, the so-called *opus caementicium* [8]. Starting from the Late Republican Age [9], they systematically employed a binder constituted of a mix of calcic lime and fine additions of amorphous silicate fractions as the structural core of their buildings, no longer constituted of loosely bound shaped stone blocks (*opus quadratum*), but by three-leaf stone masonry with externals layers acting as disposable formworks and an internal concrete infill, which guaranteed quicker construction times and higher cohesion [10]. Several Latin authors reported detailed prescriptions on the supply of raw materials, mix proportions and casting procedures, such as in Chapter 6 of the Second of the Ten Books on Architecture of Vitruvius, entirely devoted to the use of *pozzolan* in constructions [11]. Furthermore, driven by the necessity of parametrizing its production techniques, the Roman technology of pozzolanic binders relied on the systematic quarrying of the most suitable geological sources of pyroclastic materials, firstly identified in the unconsolidated pumiceous ash levels from the Phlegraean Fields volcanic district, and then, from the Augustan era on, in the loose sediments of the mid-Pleistocene *Pozzolane Rosse* pyroclastic flow from the Monti Sabatini/Alban Hills volcanic districts [12,13]. Such marked standardization led to relevant trades of raw materials throughout the Mediterranean Basin, as demonstrated in the framework of the ROMACONS project [14–16]. Nevertheless, several pieces of evidence indicated that such established supply criteria were often overcome by the employment of non-standardized local pozzolanic materials, both natural and anthropogenic (i.e. derived from anthropic processes), as a result of technological transfers with previously established productive techniques [17].

From a crystal-chemical point of view, the pozzolanic reaction products are characterized by variable composition ranging from pure, tobermorite-like C–S–H phases [18,19] to complex C–A–S–H phases at increased Al activity [20–22]. Furthermore, recent studies proved that hydraulic reaction processes can be driven outside the conventional lime-silica-alumina ternary diagram if specific conditions of alkali, magnesium and chlorine activity are satisfied. More in detail, the precipitation of zeolite-like phases is favored in complex N–K–C–A–S–H environments (where N and K stand for Na_2O and K_2O in cement chemistry notation) due to the interaction between volcanic tuffs and sea water, further enhancing the mechanical and durability properties of Roman maritime concretes [23,24]. Finally, a recent study proved that relevant precipitation of M–S–H/M–A–S–H phyllosilicate gels (where M stands for MgO in cement chemistry notation) may occur in pozzolanic binders when high magnesium, silica and alumina activities are triggered by the simultaneous employment of Mg-rich pozzolanic additives and saltwater [17].

Such complex compositional framework requires the adoption of refined multi-analytical characterization procedures for the archaeometric study of ancient pozzolanic binders, to univocally determine the chemical-physical parameters of the crystalline and amorphous structures, and the related chemical pathways inducing the cementation processes at the basis of the outstanding mechanical properties of Roman mortars and concretes [25]. This work reports the results of a multi-analytical characterization campaign on ancient pozzolanic binding composites (concretes and mortars) from the remnants of the Roman harbor of Sebastos and its nearby structures, in the archaeological site of Caesarea Maritima, Israel (in-detail archaeological information is reported in the dedicated section of the Supplementary Materials). The exceptionality of the studied context, testified by the number of archaeological and scientific studies on its materials and structures [12,15,16,25,26,27,28,29,30,31,32,33,34,35,36,37,38,39,40,41], relies on several factors:

- the high patronage of the structure, commissioned by Herod the Great in 22 BCE and sponsored by Augustus' military commander Marcus Agrippa [32,37], allowed the utilization of state-of-the-art materials and techniques for its construction, above all the first testified large-scale utilization of pumiceous pozzolanic sands imported from the Phlegraean Fields as the key building material [12,37];
- the structure is characterized by exceptional size and building complexity: constituted by two artificial moles forming three water basins (outer, intermediate, and inner harbor), it was the largest ancient artificial harbor built in the open sea, enclosing an area of around 100,000 m^2 [36,37]. This required innovative construction technologies, particularly as regards the submarine foundational structures of the moles [16,28,29,33,36,37,40];
- respectful of the cultural and technological *koine* promoted by the rising Roman empire, the project was coordinated by a heterogeneous team of engineers comprising both Roman and local Syro-Phoenician harbor builders [37,40], favoring the employment of diversified building techniques;
- binding composites were applied in diversified environments, such as fully saltwater-saturated contexts of the deep-sea foundational structures, quay areas within the tidal range, and overwater and on-land functional and religious buildings over the moles and along the coastline facing the harbor, such as vaulted storehouses and Temple of Roma and Augustus [40]. Hence, the case study monitors the influence of varying chemical-physical parameters in the mineralogical nature and structural characteristics of the anthropogenic binding phases.

Materials have been analyzed by adopting both conventional mineralogical-petrographic-microstructural approaches, fundamental to determine the nature and origin of raw materials and resulting composites, and in-detail spectroscopic studies, to parametrize the reactivity properties of the employed binding mixtures and decipher the structural characteristics of the anthropogenic cohesive compounds. The obtained results provided novel insights on reactive pathways and crystal-chemical characteristics of ancient pozzolanic binders, and ancient productive processes and technological solutions employed by Roman craftsmen to enhance the reactivity of raw materials and, consequently, performance and durability of masonry structures.

2. Materials

23 samples of binding materials were analyzed, comprising both concretes and mortars. As for the concretes, the *caementa* fraction (the Latin name for the large aggregate fraction of concrete [8]), constituted by *kurkar* rock (a local calcareous-cemented aeolianite sandstone [39]), was avoided in the sampling procedures, focusing only on their mortar component. All samples, both on-land and underwater ones, were extracted through manual removal by means of hammers and chisels from the constituting masonry elements. Five areas were sampled (Fig. 1), namely:

- Area K, at the topmost vertex of the southern mole, where five concrete breakwaters are laid in a loose header-pattern [33]. The sampling procedures were performed on an underwater concrete block still showing the wooden planks of the disposable concrete formworks (caissons [16]) (Fig. 2a). 7 concrete samples were taken in different positions at the bottom of the block. During the sampling procedures, both the poor adherence of the mortar to the *caementa* and the abundant presence of lime lumps were confirmed (Fig. 2b), as observed by [36]. All materials taken from this area were indicated with the CAE_K prefix;
- Area D, in the proximity of the internal quays of the intermediate harbor. Sampling operations were focused on the remnants of the 2.5 m-thick perimeter wall. It was built in three-leaf stone masonry technique, with an *opus caementicium* infill layer placed in-between external *opus incertum* (i.e., a masonry panel with irregular stone layers) wall facings [8], refined by *kurkar* ashlar (i.e., a shaped stone

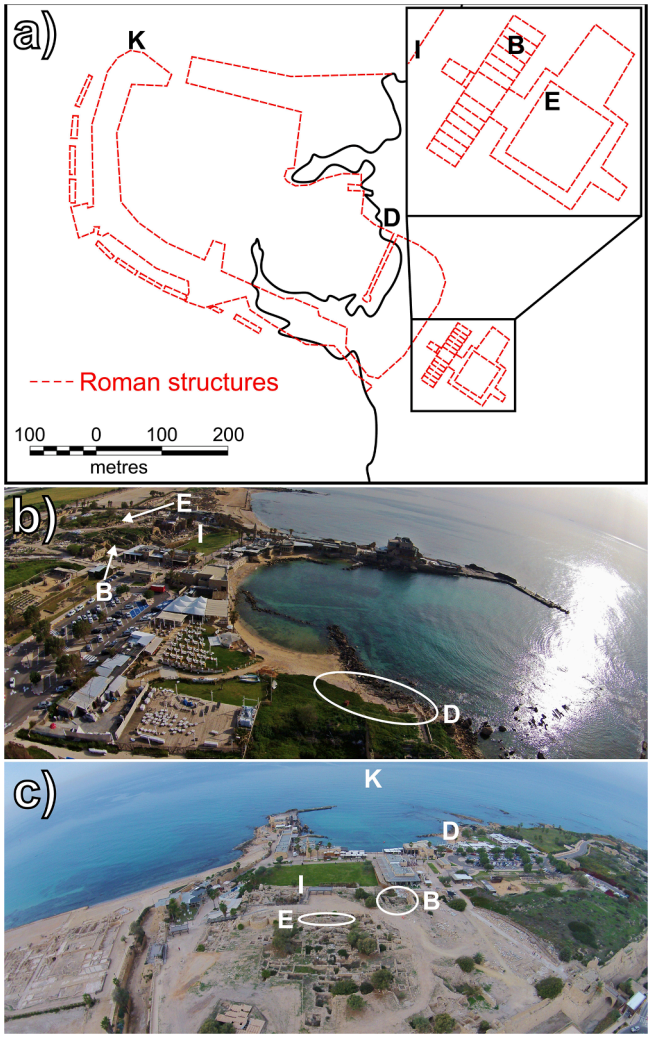

Fig. 1. a) Map of Sebastos harbor, modified after [31,33], indicating the layout of the investigated Roman structures (red dashed lines) and the five sampling areas; b) aerial view of the harbor (north to south orientation), indicating the sampling areas; c) aerial view of the harbor (east to west orientation), indicating the sampling areas. Copyright of the aerial photos: https://www.biblewalks.com. (For interpretation of the references to colour in this figure legend, the reader is referred to the web version of this article.)

block) belts in the topmost portions (Fig. 2c). Both filling concretes and mortars of the external masonry leaves (either in-between the stones of the *opus incertum* and the ashlars of the topmost belt) were sampled. Furthermore, an additional mortar sample was taken from an on-land wall parallel to the quay, built in *opus quadratum* (Fig. 2d). All samples from this area were indicated with the CAE_D prefix;

- Area I according to [31], in correspondence of the inner harbor quay in front of the Temple of Roma and Augustus. The masonry configuration of the quay in this area is constituted by a stratified foundational layer to level the irregular sandstone bedrock, refined by a superficial ashlar wall constituted of three layers of *kurkar* blocks (Fig. 2e). The configuration of the foundational layer resembles the Vitruvian floor-making prescriptions [42], being constituted by a *statumen* layer of loosely bound pottery shards, levelled by a thick mortar layer serving as a base for a *rudus* layer of coarse concrete with abundant reused blocks as *caementa* (Fig. 2f). Two samples were taken from the mortar layer between *statumen* and *rudus*, at a depth of 1 m below sea level. They were indicated with the CAE_I prefix;
- Area B, inside the remnants of the northernmost storehouses along the coastline facing the harbor. Samples were taken from the rubbles of the collapsed vaults (Fig. 2g), including both structural concretes and mortars from insulation layers on top of the vaults (Fig. 2h). All these materials were indicated with the CAE_B prefix;
- Area E, in correspondence of the foundational basement (*podium*) of the Temple of Roma and Augustus, built in *opus quadratum* (Fig. 2i). The mortars between the *kurkar* ashlars were sampled (Fig. 2j). Such group of materials was indicated with the CAE_E prefix.

The complete list of sampled materials is reported in Table 1.

3. Methods

Firstly, samples were subjected to a mineralogical clustering procedure according to the methodology described in [43,44], to group them within homogeneous compositional groups. Mineralogical analyses were performed by quantitative phase analysis on X-ray powder diffraction data (XRPD-QPA) using the Rietveld method [45]. Data were collected using a Malvern PANalytical X'Pert PRO diffractometer (Malvern PANalytical, Malvern, UK), while data analysis was performed using HighScore Plus software (Malvern PANalytical, Malvern, UK) for the qualitative interpretation of patterns, and BGMN-Profex software with dedicated fitting functions [46–50] for Rietveld refinements. Then, mineralogical clustering was obtained through a multivariate statistical treatment of the XRPD-QPA data by means of the principal component analysis (PCA) [51], performed using Origin Pro 2018 software (OriginLab Corporation, Northampton, USA).

Mineralogical data were crosschecked through petrographic, microstructural and microchemical studies on massive portions and 30 μm-thin sections of a subset of samples. Selected according to the mineralogical clustering. Petrographic analyses were performed by Transmitted Light Optical Microscopy (TL-OM) using a Nikon Eclipse ME600 microscope (Nikon Corporation, Tokyo, Japan), while microstructural and microchemical analyses were performed by Scanning Electron Microscopy (SEM-EDS) using a CamScan MX2500 microscope (CamScan, Waterbeach, UK) equipped with a LEAP + Si(Li) detector (EDAX, Mahwah, USA) for microanalysis. Qualitative interpretation of spectra and semiquantitative chemical analysis were performed through SEM Quant Phizaf software (EDAX, Mahwah, USA).

The multi-analytical characterization of the bulk samples was complemented with a combined mineralogical-spectroscopic study of their binder fractions. The study was performed on selected binder-concentrated samples obtained through a custom-modified version of the wet gravimetric separation procedure for mortars [52], as described in [17]. Materials were mineralogically characterized through XRPD-QPA, adopting the same analytical protocol used for the analysis of the bulk samples.

Then, the coordination and degree of polymerization of silicates and aluminates in the binder-concentrated samples were studied through ^{29}Si and ^{27}Al Magic-Angle Spinning Solid-State Nuclear Magnetic Resonance (MAS-SS NMR). Spectra were collected on a Bruker AVANCE III 300 spectrometer (Bruker Corporation, Billerica, USA). The signal patterns of the spectra were deconvoluted with the Peak Analyzer routine of Origin Pro 2018 software (OriginLab Corporation, Northampton, USA), using combined Gaussian-Lorentzian peak functions commonly employed for the fit of NMR data [53].

Furthermore, Fourier transform infrared spectroscopy (FTIR) was carried out on KBr pellets of the binder-concentrated samples, analyzed using a Nicolet iS5 spectrometer (Thermo Fisher Scientific, Waltham, USA). Multiple measurements of the same pellet at various particle sizes were performed according to the "grinding curve method", enabling the decoupling of local atomic disorder and optical effects [54]. The carbonate peak analysis was performed following [55], while the silicate peak analysis followed the methodology by [56].

Finally, the Total Organic Carbon (TOC) and the stable isotopic

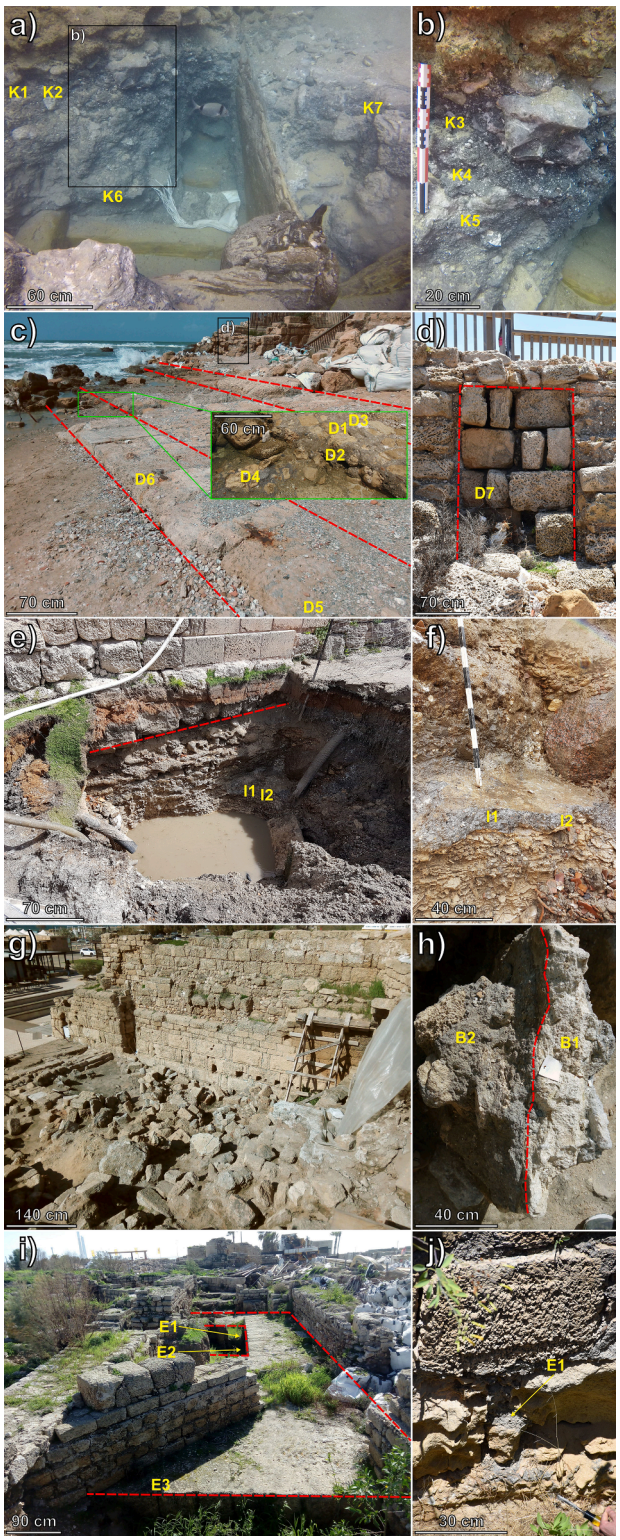

Fig. 2. a) Area K, detail of the sampled concrete block, still showing the wooden structure of the caisson used as disposable formwork. The sampling points are indicated, together with the area magnified in Fig. 2b (highlighted by the solid black rectangle marked with letter b)); b) Area K, detail of the sampled concrete reporting the sampling points; c) Area D, detail of the sampled three-leaf masonry wall constituting the internal quay of the intermediate harbor (the layout of the three leaves is highlighted by red dashed lines). Sampling points are reported, together with the area from which sample CAE_D7 was taken (highlighted by the solid black rectangle marked with the d) letter); d) Area D, detail of the sampled on-land ashlar wall (highlighted by the red dashed line). CAE_D7 sampling position is reported; e) Area I, view of the excavation site and sampling points (the red dashed line indicates the first ashlar layer of the quay); f) Area I, detail of the sampled mortar layer; g) Area B, general view; h) Area B, detail of a sampled portion of the collapsed vault (the interface between the structural concrete and the mortar of the ashlar ceiling is highlighted by the red dashed line); i) Area E, general view indicating the sampling points (the profile of the perimeter ashlar wall of the *podium* is highlighted by the red dashed lines); j) Area E, detail of CAE_E1 sampling point. (For interpretation of the references to colour in this figure legend, the reader is referred to the web version of this article.)

Table 1
List of the analyzed samples, together with their architectural and structural elements of pertinence, the adopted building technique, the type of binder and their position in relation to the current sea level.

Sample	Area	Architectural element	Structural element	Building technique	Binder type	Position
CAE_K1	K	Mole, outer harbor	Breakwater	Structural concrete	Concrete	Underwater, −8 *m*
CAE_K2	K	Mole, outer harbor	Breakwater	Structural concrete	Concrete	Underwater, −8 *m*
CAE_K3	K	Mole, outer harbor	Breakwater	Structural concrete	Concrete	Underwater, −8 *m*
CAE_K4	K	Mole, outer harbor	Breakwater	Structural concrete	Concrete	Underwater, −8.2 *m*
CAE_K5	K	Mole, outer harbor	Breakwater	Structural concrete	Concrete	Underwater, −8.4 *m*
CAE_K6	K	Mole, outer harbor	Breakwater	Structural concrete	Concrete	Underwater, −8.9 *m*
CAE_K7	K	Mole, outer harbor	Breakwater	Structural concrete	Concrete	Underwater, −7.9 *m*
CAE_D1	D	Mole, intermediate harbor	Inner quay	Stone masonry	Concrete	Intertidal
CAE_D2	D	Mole, intermediate harbor	Inner quay	Stone masonry	Concrete	Intertidal
CAE_D3	D	Mole, intermediate harbor	Inner quay	Stone masonry	Concrete	Intertidal
CAE_D4	D	Mole, intermediate harbor	Inner quay	Stone masonry	Mortar (*opus incertum*)	Intertidal
CAE_D5	D	Mole, intermediate harbor	Inner quay	Stone masonry	Mortar (ashlar)	On-land
CAE_D6	D	Mole, intermediate harbor	Inner quay	Stone masonry	Mortar (ashlar)	On-land
CAE_D7	D	Mole, intermediate harbor	Inner quay	Ashlar masonry	Mortar	On-land
CAE_I1	I	Mole, inner harbor	Inner quay	Floor bedding masonry	Mortar	Underwater, −1 *m*
CAE_I2	I	Mole, inner harbor	Inner quay	Floor bedding masonry	Mortar	Underwater, −1 *m*
CAE_B1	B	Storehouse	Vault	Structural concrete	Concrete	On-land
CAE_B2	B	Storehouse	Vault	Structural concrete	Mortar	On-land
CAE_B3	B	Storehouse	Vault	Structural concrete	Concrete	On-land
CAE_B4	B	Storehouse	Vault	Structural concrete	Mortar	On-land
CAE_E1	E	Temple	Foundational basement	Ashlar masonry	Mortar	On-land
CAE_E2	E	Temple	Foundational basement	Ashlar masonry	Mortar	On-land
CAE_E3	E	Temple	Foundational basement	Ashlar masonry	Mortar	On-land

composition of organic carbon ($\delta^{13}C$) were determined on the binder-concentrated samples. TOC analyses were performed using a Thermo Scientific Flash 2000 Elemental Analyzer (Thermo Fisher Scientific, Waltham, USA), and the obtained C contents were interpreted as the amount of organic carbon (i.e. charcoal) within each analyzed sample. $\delta^{13}C$ measurements, normalized to the standard Vienna Pee Dee Belemnite (VPDB) scale [57] were performed on a Thermo Delta V Advantage Isotopic Ratio Mass Spectrometer (Thermo Fisher Scientific, Waltham, USA). The same instrument was used for the $\delta^{13}C$ and $\delta^{18}O$ analyses on the inorganic carbonate fractions. All isotopic results were calibrated with two internal standards (sieved Carrara marble and Millipore Suprapur® carbonate), which are in turn periodically calibrated against the international reference carbonates NBS 19; NBS 18 and L-SVEC [58].

A detailed description of the sample preparation procedures, instrumental parameters, and methodologies of data analysis is reported in the dedicated section of the Supplementary Materials.

4. Results

4.1. Mineralogical characterization

The quantitative mineralogical profiles of the analyzed samples are reported in Table 2, while the results of the PCA are reported in Fig. 3a through the scatterplot (biplot) of the first two principal components (PC1 and PC2), obtained after log-transformation of the quantitative mineralogical data, and cumulatively representing 59.10 % of the whole dataset variance. The statistical treatment of the data allowed clustering the samples into three distinct Mineralogical Groups:

- **Group 1**, characterized by positive PC1 values. Such group comprises the concrete samples, either from the breakwater concrete block, the intermediate harbor quay or the storehouses vaults, and the mortar of the on-land ashlar wall close to the intermediate harbor quay. These samples are characterized by a positive correlation with a comparable assemblage of silicate phases typical for pyroclastic products [59], namely sodic sanidine, plagioclase of labradoritic composition, biotite, augite and zeolites (Na/K-phillipsite, analcime and chabazite). The sole significant discrepancy is related to the occurrence of relevant Na/K-phillipsite aliquots in some of the samples, such as CAE_D2, where the zeolite constitutes the dominant phase of the mineralogical assemblage. Despite such similarities, the samples of this group are characterized by significant variations in their three major components, namely calcite, amorphous phase, and structurally disordered smectite-like phyllosilicate gels (Fig. 3b, 4). The relative amounts of these main components allowed a further subdivision into three sub-groups (Fig. 3b): i) **1a** (CAE_K1, CAE_K2, CAE_K3, CAE_K7, CAE_D2), characterized by calcite amounts lower than 20 wt% (mean value: 14.45 wt%) and comparable amounts of phyllosilicate gels and amorphous phase (mean values of 22.78 wt% and 23.70 wt%, respectively); ii) **1b** (CAE_K4, CAE_K5, CAE_K6, CAE_D1, CAE_D3), characterized by higher amounts of calcite and amorphous phase (mean values of 22.27 wt% and 34.36 wt%, respectively) and fewer phyllosilicate gels (mean value: 9.86 wt%); iii) **1c** (CAE_B1, CAE_B3), characterized by the highest calcite and amorphous phase values (mean values of 26.91 wt% and 38.57 wt%, respectively) and almost no phyllosilicate gels (mean value: 2.92 wt %). Sample CAE_D7 is an outlier, mainly due to the presence of relevant quartz amounts, whose occurrence is limited in the other samples. Furthermore, samples are characterized by the occurrence of limited amounts of gypsum and halite. Finally, concrete samples taken from the breakwater block are characterized by reduced pyrite content, which is larger in samples from sub-group 1a.
- **Group 2**, characterized by negative PC1 and PC2 values. Such group comprises the remaining mortar samples, apart from the ones in-between the ashlars of the topmost belt of the intermediate harbor quay. Such samples are characterized by the occurrence of higher calcite amounts with respect to the ones of the previous group, and aragonite amounts ranging from 1.13 wt% of CAE_E1 to 6.81 wt% of CAE_B4. Furthermore, they are devoid of silicate phases of pyroclastic origin, while quartz is present in significant amounts, associated to reduced quantities of microcline and anorthite feldspars. Phyllosilicate gels are present in relevant amounts only in mortar samples of the quays (Fig. 3b), and the amounts of amorphous phase are comparable to those of sub-group 1a (mean value: 21.41 wt%). Finally, some of the samples present reduced halite aliquots, and sample CAE_I1 contains lizardite and dolomite, the latter with a reduced crystallite size and a high degree of structural disorder.
- **Group 3**, characterized by negative PC1 and positive PC2 values. Such group includes the two mortar samples taken in-between the ashlars of the topmost belt of the intermediate harbor quay. Despite the occurrence of labradoritic plagioclase and, for CAE_D6, augite,

Table 2
Mineralogical quantitative phase analysis of the analyzed bulk samples, obtained by full profile fitting of the experimental XRPD patterns according to the Rietveld method (estimated standard deviations are reported in brackets).

Sample	Calcite	Aragonite	Mg-calcite	Dolomite	Quartz	Na-sanidine	Microcline	Labradorite	Anorthite	Augite	Analcime	Chabazite	Na/K-phillipsite	Biotite	Lizardite	Phyllosilicate gel	Gypsum	Pyrite	Halite	Amorphous
CAE_K1	8.43 (0.16)	0.00 (0.00)	0.00 (0.00)	0.00 (0.00)	1.99 (0.07)	16.06 (0.36)	0.00 (0.00)	2.35 (0.28)	0.00 (0.00)	1.9 (0.24)	2.20 (0.08)	0.99 (0.16)	1.98 (0.18)	2.31 (0.11)	0.00 (0.00)	23.31 (0.74)	0.93 (0.09)	0.45 (0.05)	0.44 (0.04)	36.70 (1.10)
CAE_K2	16.33 (0.22)	0.00 (0.00)	0.00 (0.00)	0.00 (0.00)	1.45 (0.06)	15.33 (0.38)	0.00 (0.00)	1.57 (0.21)	0.00 (0.00)	0.85 (0.16)	1.53 (0.08)	0.66 (0.14)	2.10 (0.19)	2.63 (0.12)	0.00 (0.00)	24.46 (0.78)	0.00 (0.00)	0.42 (0.05)	0.34 (0.04)	32.30 (1.10)
CAE_K3	25.53 (0.23)	0.00 (0.00)	0.00 (0.00)	0.00 (0.00)	9.23 (0.10)	11.11 (0.40)	0.00 (0.00)	2.87 (0.22)	0.00 (0.00)	2.04 (0.16)	2.63 (0.10)	2.12 (0.13)	10.43 (0.28)	0.58 (0.09)	0.00 (0.00)	16.69 (0.72)	0.32 (0.06)	0.26 (0.05)	0.79 (0.05)	15.40 (1.10)
CAE_K4	26.56 (0.29)	0.00 (0.00)	0.00 (0.00)	0.00 (0.00)	2.12 (0.08)	14.02 (0.45)	0.00 (0.00)	5.10 (0.34)	0.00 (0.00)	0.00 (0.00)	2.41 (0.11)	1.03 (0.13)	2.03 (0.20)	1.31 (0.10)	0.00 (0.00)	11.62 (0.86)	1.05 (0.09)	0.20 (0.03)	0.92 (0.05)	31.60 (1.20)
CAE_K5	24.25 (0.20)	0.00 (0.00)	0.00 (0.00)	0.00 (0.00)	3.07 (0.05)	15.91 (0.32)	0.00 (0.00)	3.07 (0.28)	0.00 (0.00)	1.88 (0.15)	2.84 (0.08)	0.31 (0.09)	1.62 (0.21)	1.15 (0.10)	0.00 (0.00)	9.38 (0.86)	1.08 (0.07)	0.13 (0.04)	0.64 (0.04)	34.70 (1.10)
CAE_K6	22.08 (0.24)	0.00 (0.00)	0.00 (0.00)	0.00 (0.00)	3.22 (0.07)	17.18 (0.40)	0.00 (0.00)	3.17 (0.29)	0.00 (0.00)	2.25 (0.17)	3.12 (0.09)	0.22 (0.09)	1.14 (0.17)	1.05 (0.09)	0.00 (0.00)	5.12 (0.5)	1.80 (0.11)	0.07 (0.06)	1.08 (0.05)	38.52 (0.84)
CAE_K7	10.48 (0.21)	0.00 (0.00)	0.00 (0.00)	0.00 (0.00)	1.38 (0.06)	15.27 (0.48)	0.00 (0.00)	3.98 (0.39)	0.00 (0.00)	1.35 (0.24)	1.24 (0.09)	0.00 (0.00)	8.75 (0.26)	2.74 (0.17)	0.00 (0.00)	35.26 (0.84)	0.57 (0.07)	0.42 (0.05)	0.54 (0.06)	18.00 (1.20)
CAE_D1	21.46 (0.21)	0.00 (0.00)	0.00 (0.00)	0.00 (0.00)	4.26 (0.07)	14.25 (0.37)	0.00 (0.00)	4.05 (0.36)	0.00 (0.00)	2.04 (0.16)	2.61 (0.08)	0.78 (0.12)	5.71 (0.20)	0.77 (0.09)	0.00 (0.00)	10.32 (0.71)	0.57 (0.08)	0.00 (0.00)	2.10 (0.06)	31.10 (1.00)
CAE_D2	11.47 (0.23)	0.00 (0.00)	0.00 (0.00)	0.00 (0.00)	3.38 (0.08)	12.61 (0.40)	0.00 (0.00)	4.74 (0.39)	0.00 (0.00)	2.61 (0.19)	0.84 (0.09)	1.16 (0.13)	28.47 (0.39)	2.01 (0.13)	0.00 (0.00)	14.17 (0.72)	0.00 (0.00)	0.00 (0.00)	2.45 (0.08)	16.10 (1.2)
CAE_D3	17.01 (0.20)	0.00 (0.00)	0.00 (0.00)	0.00 (0.00)	5.83 (0.08)	11.84 (0.39)	0.00 (0.00)	3.18 (0.17)	0.00 (0.00)	1.61 (0.17)	1.40 (0.09)	0.43 (0.10)	5.64 (0.17)	0.94 (0.09)	0.00 (0.00)	12.87 (0.64)	0.55 (0.06)	0.00 (0.00)	2.53 (0.06)	36.16 (0.89)
CAE_D4	46.55 (0.3)	3.00 (0.15)	0.00 (0.00)	0.00 (0.00)	11.21 (0.10)	0.00 (0.00)	1.85 (0.14)	0.00 (0.00)	1.06 (0.11)	0.00 (0.00)	0.00 (0.00)	0.00 (0.00)	0.00 (0.00)	0.00 (0.00)	0.00 (0.00)	10.02 (0.67)	0.00 (0.00)	0.00 (0.00)	1.60 (0.06)	24.71 (0.87)
CAE_D5	18.07 (0.29)	4.25 (0.18)	14.41 (0.65)	9.40 (0.18)	5.91 (0.08)	0.00 (0.00)	0.00 (0.00)	2.59 (0.12)	0.00 (0.00)	0.00 (0.00)	0.00 (0.00)	0.00 (0.00)	0.00 (0.00)	0.00 (0.00)	0.00 (0.00)	8.39 (0.40)	0.91 (0.08)	0.00 (0.00)	3.15 (0.11)	32.93 (0.88)
CAE_D6	31.07 (0.41)	24.09 (0.21)	4.33 (0.36)	0.00 (0.00)	4.81 (0.06)	0.10 (0.16)	0.00 (0.00)	3.70 (0.13)	0.00 (0.00)	0.81 (0.21)	0.00 (0.00)	0.00 (0.00)	0.00 (0.00)	0.00 (0.00)	0.00 (0.00)	4.36 (0.66)	0.00 (0.00)	0.00 (0.00)	1.82 (0.09)	24.91 (0.94)
CAE_D7	16.44 (0.17)	0.00 (0.00)	0.00 (0.00)	0.00 (0.00)	20.12 (0.14)	12.61 (0.35)	0.00 (0.00)	3.53 (0.31)	0.00 (0.00)	0.67 (0.20)	2.00 (0.10)	0.29 (0.09)	1.20 (0.14)	0.54 (0.09)	0.00 (0.00)	2.30 (0.48)	1.61 (0.09)	0.00 (0.00)	4.85 (0.15)	33.84 (0.83)
CAE_I1	47.08 (0.28)	1.61 (0.15)	0.00 (0.00)	1.5 (0.1)	17.45 (0.13)	0.00 (0.00)	1.20 (0.16)	0.00 (0.00)	1.09 (0.12)	0.00 (0.00)	0.00 (0.00)	0.00 (0.00)	0.00 (0.00)	0.00 (0.00)	1.11 (0.11)	8.64 (0.78)	0.00 (0.00)	0.00 (0.00)	0.00 (0.00)	20.31 (0.95)
CAE_I2	28.27 (0.22)	3.13 (0.15)	0.00 (0.00)	0.00 (0.00)	34.36 (0.21)	0.00 (0.00)	1.73 (0.18)	0.00 (0.00)	2.11 (0.12)	0.00 (0.00)	0.00 (0.00)	0.00 (0.00)	0.00 (0.00)	0.00 (0.00)	0.00 (0.00)	5.50 (0.71)	0.00 (0.00)	0.00 (0.00)	0.00 (0.00)	24.91 (0.90)
CAE_B1	28.44 (0.23)	0.00 (0.00)	0.00 (0.00)	0.00 (0.00)	4.14 (0.07)	11.99 (0.37)	0.00 (0.00)	3.02 (0.38)	0.00 (0.00)	2.33 (0.19)	1.15 (0.08)	0.96 (0.06)	3.67 (0.23)	1.49 (0.08)	0.00 (0.00)	5.84 (0.44)	0.00 (0.00)	0.00 (0.00)	0.00 (0.00)	36.97 (0.83)
CAE_B2	37.05 (0.27)	6.84 (0.24)	0.00 (0.00)	0.00 (0.00)	37.20 (0.24)	0.00 (0.00)	1.77 (0.17)	0.00 (0.00)	2.04 (0.12)	0.00 (0.00)	0.00 (0.00)	0.00 (0.00)	0.00 (0.00)	0.00 (0.00)	0.00 (0.00)	0.00 (0.00)	0.00 (0.00)	0.00 (0.00)	0.00 (0.00)	15.11 (0.58)
CAE_B3	25.37 (0.22)	0.00 (0.00)	0.00 (0.00)	0.00 (0.00)	5.00 (0.07)	17.47 (0.35)	0.00 (0.00)	2.01 (0.24)	0.00 (0.00)	2.73 (0.17)	2.12 (0.08)	1.09 (0.07)	2.90 (0.15)	1.15 (0.08)	0.00 (0.00)	0.00 (0.00)	0.00 (0.00)	0.00 (0.00)	0.00 (0.00)	40.16 (0.54)
CAE_B4	42.86 (0.29)	6.81 (0.20)	0.00 (0.00)	0.00 (0.00)	22.88 (0.17)	0.00 (0.00)	0.97 (0.19)	0.00 (0.00)	0.79 (0.09)	0.00 (0.00)	0.00 (0.00)	0.00 (0.00)	0.00 (0.00)	0.00 (0.00)	0.00 (0.00)	0.00 (0.00)	0.00 (0.00)	0.00 (0.00)	0.34 (0.06)	25.35 (0.51)
CAE_E1	37.18 (0.27)	1.13 (0.11)	0.00 (0.00)	0.00 (0.00)	29.71 (0.20)	0.00 (0.00)	1.67 (0.19)	0.00 (0.00)	2.11 (0.15)	0.00 (0.00)	0.00 (0.00)	0.00 (0.00)	0.00 (0.00)	0.00 (0.00)	0.00 (0.00)	2.04 (0.44)	0.00 (0.00)	0.00 (0.00)	1.16 (0.14)	25.00 (0.72)
CAE_E2	40.90 (0.28)	1.39 (0.12)	0.00 (0.00)	0.00 (0.00)	29.78 (0.19)	0.00 (0.00)	1.71 (0.17)	0.00 (0.00)	2.51 (0.13)	0.00 (0.00)	0.00 (0.00)	0.00 (0.00)	0.00 (0.00)	0.00 (0.00)	0.00 (0.00)	5.07 (0.39)	0.00 (0.00)	0.00 (0.00)	0.59 (0.04)	18.06 (0.65)
CAE_E3	56.60 (0.33)	3.43 (0.15)	0.00 (0.00)	0.00 (0.00)	19.48 (0.14)	0.00 (0.00)	0.83 (0.14)	0.00 (0.00)	1.80 (0.12)	0.00 (0.00)	0.00 (0.00)	0.00 (0.00)	0.00 (0.00)	0.00 (0.00)	0.00 (0.00)	0.00 (0.00)	0.00 (0.00)	0.00 (0.00)	0.00 (0.00)	17.86 (0.47)

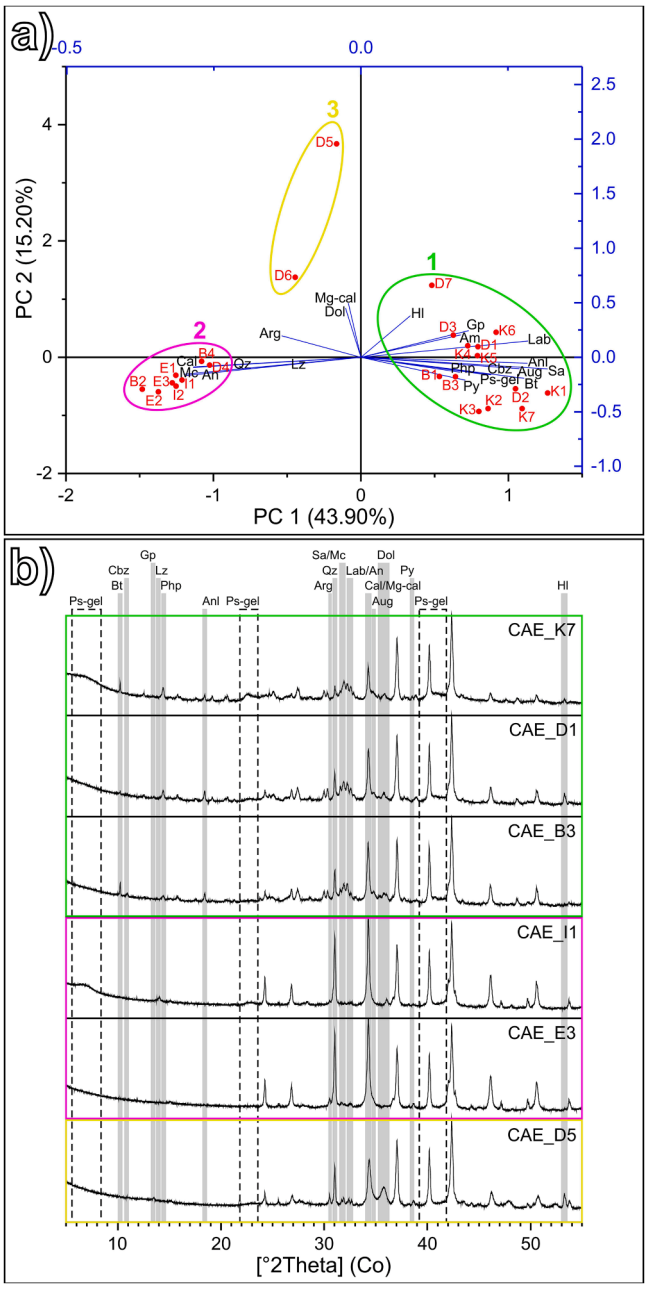

Fig. 3. a) Biplot of the principal component analysis of the mineralogical quantitative data obtained from the analyzed bulk samples (data are reported in Table 2): the first two components have been plotted, representing 59.10 % of the total variance. The three defined Mineralogical Groups are indicated by colored ellipses; b) XRPD patterns of representative samples for each defined group (the main diffraction peaks of the mineral phases are highlighted). Abbreviations: Ps-gel = phyllosilicate gels, Bt = biotite, Cbz = chabazite, Gp = gypsum, Lz = lizardite, Php = Na/K-phillipsite, Anl = analcime, Arg = aragonite, Qz = quartz, Sa = Na-sanidine, Mc = microcline, Lab = labradorite, An = anorthite, Cal = calcite, Mg-cal = magnesian calcite, Aug = augite, Dol = dolomite, Py = pyrite, Hl = halite.

such materials are lacking further silicate phases of pyroclastic origin detected in the samples of group 1. Furthermore, apart from the occurrence of calcite, both samples present relevant aragonite contents, reaching values over 20 wt% in CAE_D6, and they are both characterized by the presence of magnesian calcite. Also, sample CAE_D5 is rich in a low-crystalline, structurally disordered form of dolomite (Fig. 3b). Both samples present comparable amounts of

Table 3
Mineralogical quantitative phase analysis of the selected binder-concentrated samples for Groups 1 and 2, obtained by full profile fitting of the experimental XRPD patterns according to the Rietveld method (estimated standard deviations are reported in brackets).

Sample	Calcite	Aragonite	Ca-AFm	Quartz	Na-sanidine	Augite	Analcime	Chabazite	Phyllosilicate gel	Hydroxyapatite	Gypsum	Halite	Amorphous
CAE_K2	0.49 (0.13)	0.00 (0.00)	0.00 (0.00)	0.00 (0.00)	2.17 (0.33)	0.00 (0.00)	0.00 (0.00)	0.00 (0.00)	56.96 (0.35)	0.00 (0.00)	0.00 (0.00)	0.00 (0.00)	40.37 (2.64)
CAE_K4	2.44 (0.20)	0.00 (0.00)	0.00 (0.00)	0.30 (0.07)	1.86 (0.22)	0.00 (0.00)	0.26 (0.11)	0.00 (0.00)	39.10 (1.2)	0.00 (0.00)	0.71 (0.08)	0.00 (0.00)	55.33 (2.70)
CAE_K7	0.67 (0.31)	0.00 (0.00)	0.00 (0.00)	0.00 (0.00)	2.09 (0.34)	0.00 (0.00)	0.00 (0.00)	0.00 (0.00)	57.25 (0.46)	0.00 (0.00)	0.00 (0.00)	0.00 (0.00)	40.00 (3.10)
CAE_D4	12.70 (0.31)	1.49 (0.16)	0.00 (0.00)	0.26 (0.07)	0.00 (0.00)	0.00 (0.00)	0.00 (0.00)	0.00 (0.00)	39.10 (1.10)	0.43 (0.18)	0.00 (0.00)	0.00 (0.00)	46.00 (1.30)
CAE_I1	14.45 (0.29)	1.20 (0.13)	0.16 (0.09)	0.00 (0.00)	0.00 (0.00)	0.00 (0.00)	0.00 (0.00)	0.00 (0.00)	46.40 (1.10)	0.91 (0.20)	0.00 (0.00)	0.00 (0.00)	36.90 (1.20)
CAE_B3	13.40 (0.23)	0.00 (0.00)	0.00 (0.00)	0.37 (0.05)	1.59 (0.15)	1.53 (0.18)	0.00 (0.00)	0.39 (0.06)	0.00 (0.00)	0.00 (0.00)	0.00 (0.00)	2.55 (0.08)	80.18 (0.35)
CAE_E2	20.64 (0.25)	0.46 (0.09)	0.00 (0.00)	0.27 (0.05)	0.00 (0.00)	0.00 (0.00)	0.00 (0.00)	0.00 (0.00)	15.99 (0.70)	0.71 (0.17)	0.00 (0.00)	0.00 (0.00)	61.93 (0.83)

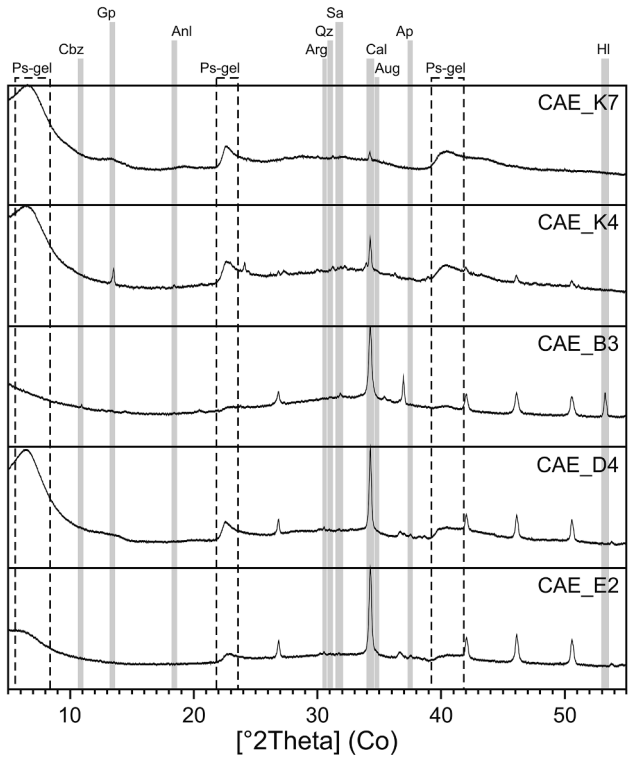

Fig. 4. XRPD patterns of representative binder-concentrated samples for Groups 1 and 2 (data are reported in Table 3). Main diffraction peaks of the mineral phases are highlighted. Abbreviations: Ps-gel = phyllosilicate gels, Cbz = chabazite, Gp = gypsum, Anl = analcime, Arg = aragonite, Qz = quartz, Sa = Na-sanidine, Cal = calcite, Aug = augite, Ap = hydroxyapatite, Hl = halite.

quartz, affine to the ones detected in group 1 materials, while the amounts of phyllosilicate gels and amorphous phase are higher in CAE_D5. Finally, both mortars contain halite, and reduced aliquots of gypsum are present in CAE_D5.

Mineralogical analyses on binder-concentrated samples of selected materials (Table 3, Fig. 4) gave results in line with those obtained from bulk samples. Group 1a samples (CAE_K2, CAE_K7) are almost exclusively composed of phyllosilicate gels and amorphous fraction, with higher proportions of the former component. Calcite is almost absent, as are aggregate minerals. The analyzed sample from Group 1b (CAE_K4) presents higher calcite content, dominant phyllosilicate gels and amorphous fraction, the latter being the most abundant. Furthermore, traces of minerals related to the aggregate fraction are present, together with reduced amounts of gypsum. The reference sample from Group 1c (CAE_B3) presents relevant calcite content and a dominant amorphous fraction, while phyllosilicate gels are absent. Small residues of aggregate-related minerals are present, together with limited halite. Samples of Group 2 present the same heterogeneities observed in the bulk materials: the binder-concentrated samples from the quays present a calcite content comparable to that of Group 1c sample, with dominant fractions of phyllosilicate gels and amorphous phase. Sample CAE_E2 from the bedding mortar of the Temple *podium* presents the highest calcite concentrations, a dominant amorphous fraction, and lower amounts of phyllosilicate gels with respect to the other samples of the same group. Furthermore, all samples present traces of the aggregate minerals, and samples CAE_D4, CAE_I1 and CAE_E2 contain reduced amounts of aragonite and hydroxyapatite. Finally, sample CAE_I1 contains traces of a poorly crystalline Ca-based carboaluminate Afm phase, a typical C–A–H pozzolanic reaction product of ancient hydraulic binders [42].

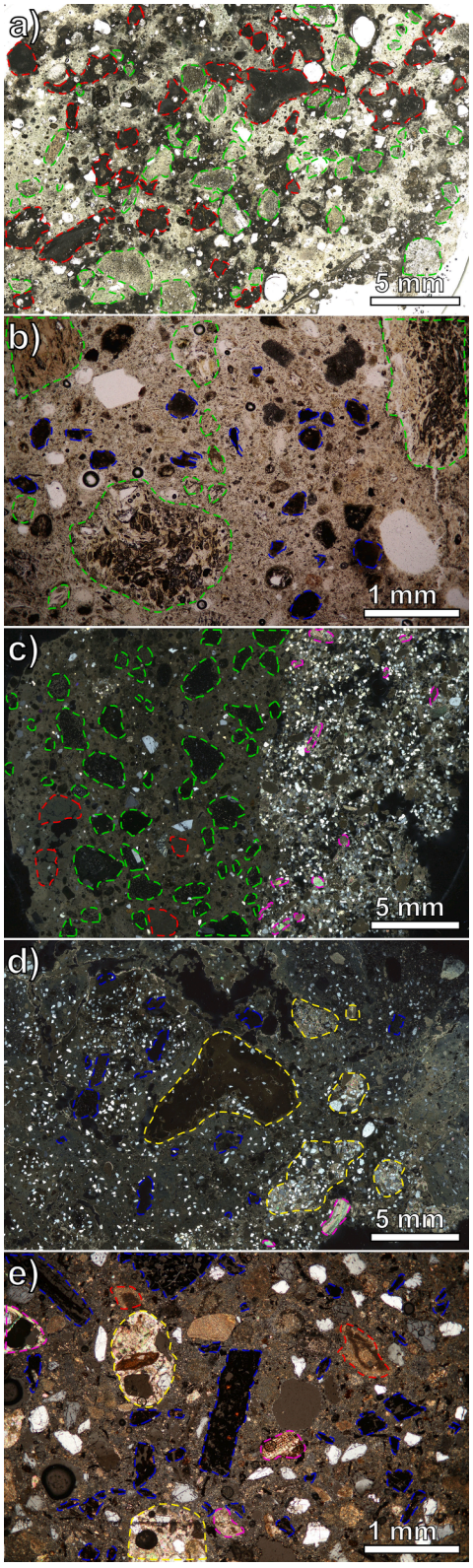

Fig. 5. Selected TL-OM micrographs of the analyzed samples: a) sample CAE_K2, plane polars; b) sample CAE_K2, plane polars; c) sample CAE_B3 (to the left) and CAE B4 (to the right), crossed polars; d) sample CAE_E4, crossed polars; e) sample CAE_I1, crossed polars. The main classes of particles have been highlighted by colored dashed lines: lime lumps in red, pyroclastic aggregates in green, combustion residues in blue, terrigenous aggregates in yellow, shell fragments in magenta. (For interpretation of the references to colour in this figure legend, the reader is referred to the web version of this article.)

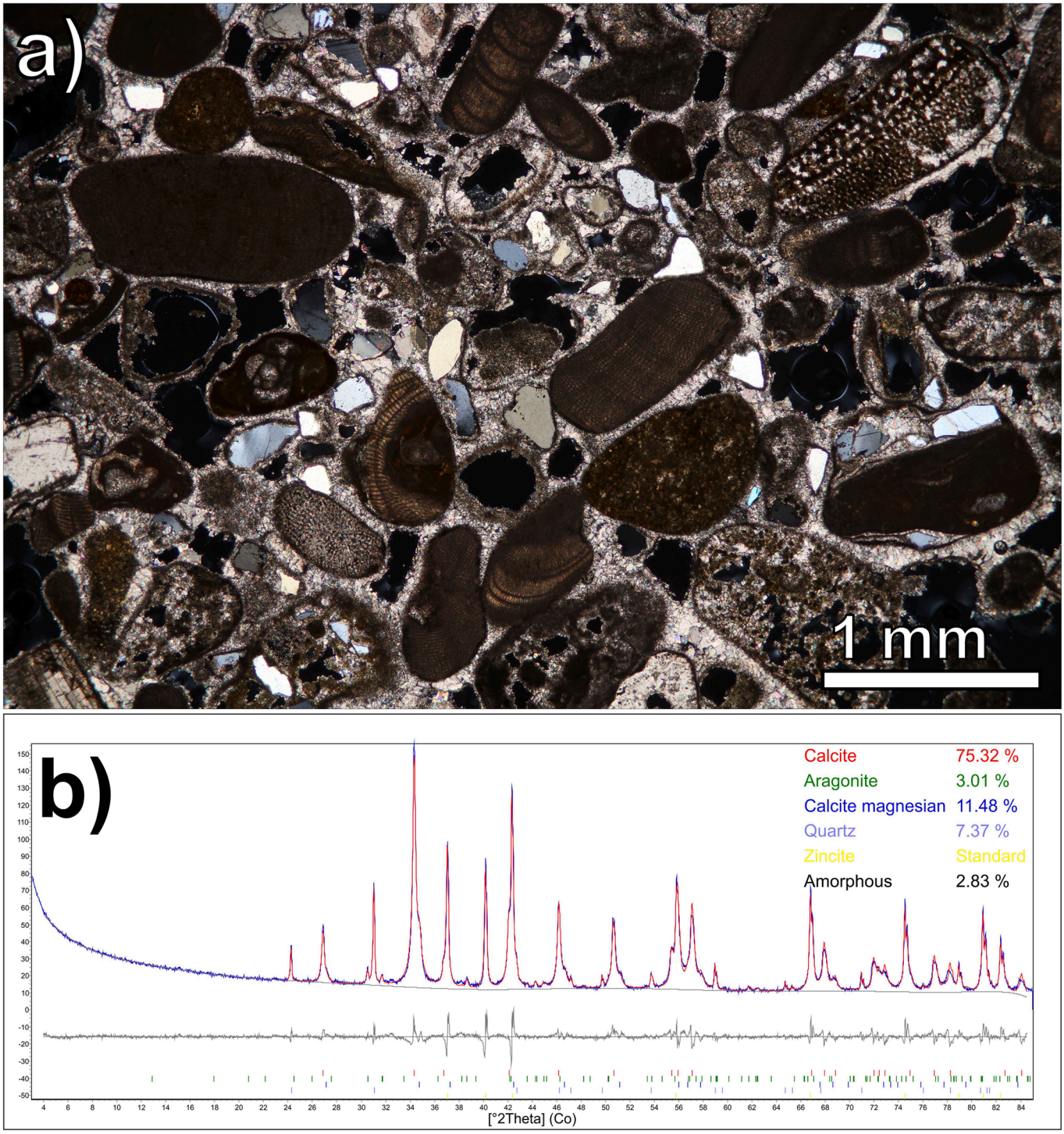

Fig. 6. a) TL-OM micrograph (crossed polars) of a portion of *kurkar* ashlar sampled in the Caesarea Maritima archaeological site; b) XRPD pattern and results of the XRPD-QPA of the analyzed stone sample.

4.2. Petrographic, microstructural and microchemical characterization

Microscopic analyses (see Figs. 5-11) highlighted the occurrence of four different types of sandy aggregate fractions in the analyzed binding composites, whose occurrence is differentiated according to the mineralogical group of pertinence:

- **Pyroclastic aggregates**. These aggregates are present in the samples of Groups 1 and 3. They are constituted of subrounded to rounded particles of white-greenish pumice and yellowish tuff (Fig. 5a, 5b, 5c), with dimensions ranging from very coarse to fine sands [60]. Pumice clasts are in form of vesicular hypocrystalline aggregates (Fig. 8), with scarce sanidine phenocrysts and a glassy fraction of silico-aluminous-potassic composition with traces of sodium, chlorine, calcium, titanium and iron (Fig. 8c, 8 k). Tuff particles present a hypocrystalline texture, with a partially zeolitized cineritic matrix embedding sanidine microlites (Fig. 8g) and scarce plagioclase, clinopyroxene and biotite phenocrysts. Pyroclastic aggregates present extensive dissolution features in samples of Groups 1a, 1b and 3, with a pervasive reaction of the glassy matrix of pumices up to the

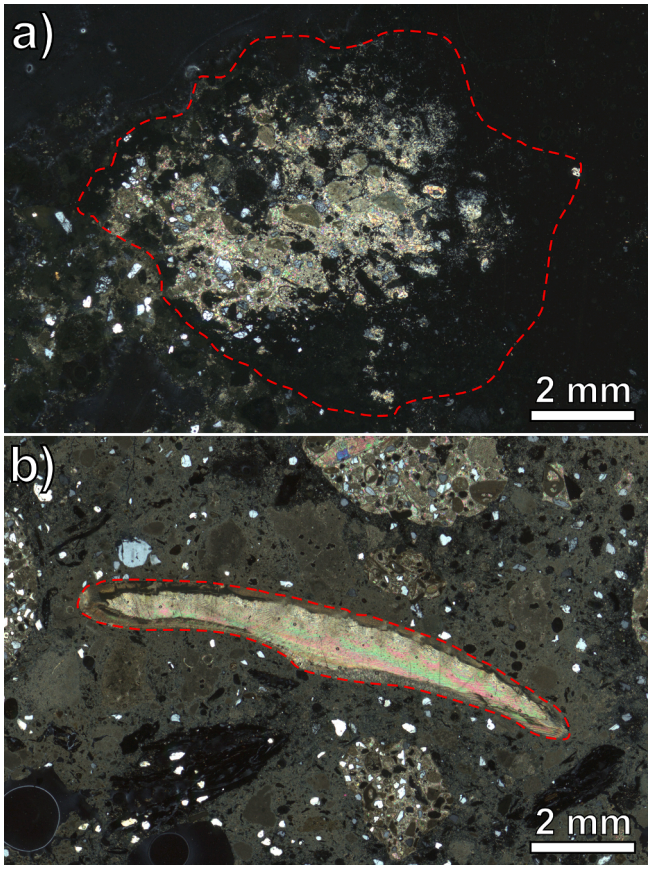

Fig. 7. a) Sample CAE_D1, TL-OM micrograph (crossed polars) of a *kurkar* aggregate grain showing extensive interfacial dissolution features (the original margin of the particle is highlighted by the red dashed line); b) Sample CAE_I1, TL-OM micrograph (crossed polars) of a shell fragment characterized by the occurrence of an interfacial dissolution rim (the original margin of the particle is highlighted by the red dashed line).

core of millimetre-sized aggregates (Fig. 8a, 8b), and permanence of the sole microlites and phenocrysts in the tuff fragments (Fig. 8e, 8f). Pseudomorphic reaction products within reacted clasts present a silico-magnesian-aluminous composition, associated to chlorine, calcium and traces of alkalis, sulfur and iron (Fig. 8d, 8 h). Dissolution of pyroclastic aggregates is less pervasive in the samples of Group 1c, with extensive reaction circumscribed to the smallest and more porous particles and to interfacial portions of the coarser clasts (Fig. 8i, 8j). Pseudomorphic reaction products within the volcanic aggregates present a silico-calcic-aluminous composition, associated to potassium and traces of sodium, chlorine and iron (Fig. 8l).

- **Combustion residues**. These aggregates are present in all samples except those of Group 1c, with a greater abundance in samples of Group 2. They are constituted of subangular to subrounded ash and charcoal particles derived from organic matter combustion (Fig. 5b, 5d, 5e), with dimensions ranging from coarse to very fine sands [60]. Charcoal particles are quantitatively subordinate with respect to the ash component, and they often retain the cellular shapes of vegetal species (Fig. 5e, 9a), with abundant filling of the vacuoles with anthropogenic calcium carbonates (Fig. 9b). The smallest ash clusters are constituted of homogeneous matrices of cryptocrystalline particles (Fig. 9c, 9e), mainly siliceous-aluminous-magnesian-calcic in composition, with reduced local concentrations of calcium and phosphorus likely related to the occurrence of calcium phosphates, and traces of alkalis, chlorine and iron (Fig. 9d, 9f). Coarser ash clusters present more heterogeneous textures (Fig. 9g, 9i), with highly siliceous cryptocrystalline matrices (Fig. 9h) embedding larger charcoal and quartz grains and scarce localized portions of calcic-phosphatic composition (Fig. 9j). Aggregates present extensive interfacial dissolution features.
- **Terrigenous aggregates**. These aggregates are abundantly present in samples of Group 2 and in sample CAE_D7 (Fig. 5c, 5d, 5e), but they are detectable in lower amounts also in samples of Group 1, likely as residual sandy fractions of the *caementa* constituents of concrete. They are constituted of subangular quartz particles with dimensions ranging from medium to fine sands [60] and subrounded calcareous-cemented aeolianite sandstone fragments with dimensions ranging from fine gravels to coarse sands [60]. Rock fragments show petrographic, textural, and mineralogical features fully consistent with those of the local *kurkar* stone, i.e. a grainstone [61] with abundant carbonate bioclasts and ooids and subordinate aeolian quartz grains, cemented by a sparry carbonate cement (Fig. 6a), with a mineralogical composition given by dominant calcite and relevant proportions of magnesian calcite, together with quartz and aragonite (Fig. 6b). While quartz grains are devoid of interfacial dissolution features, grainstone fragments within underwater and intertidal samples of Groups 1 and 2 are frequently characterized by the occurrence of relevant dissolution rims (Fig. 7a).
- **Shell fragments**. These aggregates are present in samples of Group 2 (Fig. 5c, 5d, 5e). They are elongated shell fragments of *Bivalvia* mollusks with carbonate composition, and dimensions ranging from fine gravels to medium sands [60]. These aggregates are devoid of interfacial dissolution features in the samples related to on-land structures, while they are often characterized by the occurrence of dissolution rims in the materials sampled from underwater and intertidal portions (Fig. 7b).

The microstructural and microchemical characteristics of the binding matrices in the analyzed samples are heterogeneous, in accordance with the mineralogical clusters defined through XRPD-QPA. Materials of Groups 1a and 1b present matrices rich in capillary pores, constituted of dense clusters of optically-extinct cryptocrystalline particles, homogeneous in composition (Fig. 10a). These are composed of dominant silicon and magnesium, associated to aluminum and traces of chlorine (Fig. 10c). Calcium is present in small quantities, mainly concentrated within lumps with dimensions ranging from hundreds of micrometers to a few millimeters (Fig. 10a, 10b, 10d), and it is present in greater amounts in samples of Group 1b. Sometimes, lumps are characterized by spheroidal shapes with increasing amounts of calcium towards the nuclei (Fig. 10a). Furthermore, there are numerous micrometric euhedral particles, opaque at TL-OM analysis and characterized by intense backscattered electrons (BSE) signal at the SEM (Fig. 11), whose chemical composition given by dominant sulfur and iron identify them as pyrite crystals (Fig. 11c). These are both scattered within the binding matrices, and preferentially accumulated in the nuclei of the spheroidal Ca-rich lumps and along the margins of pumice and tuff particles, also characterized by calcium enrichments with respect to the matrices.

Samples of Group 1c present binding matrices rich in capillary pores and composed of clusters of cryptocrystalline particles, despite resulting more heterogeneous in texture and composition (Fig. 10e, 10f). Optically-extinct areas are diffuse, mainly composed of calcium and silicon in comparable amounts, with associated aluminum, alkalis and traces of iron, magnesium and chlorine (Fig. 10g). Nevertheless, a relevant occurrence of portions characterized by interference colors closer to those of calcite, richer in calcium is observable (Fig. 10*h*). Furthermore, few millimetric lime lumps are present (Fig. 10e), and the capillary porosity is often filled by calcite-based compounds (Fig. 10e, 10f).

Samples of group 2 from terrestrial structures present binding matrices with similar characteristics to those of group 1c, with lower aluminum and slightly higher magnesium contents (Fig. 10i, 10j, 10 k, 10 l). On the contrary, materials related to the quays resemble those of

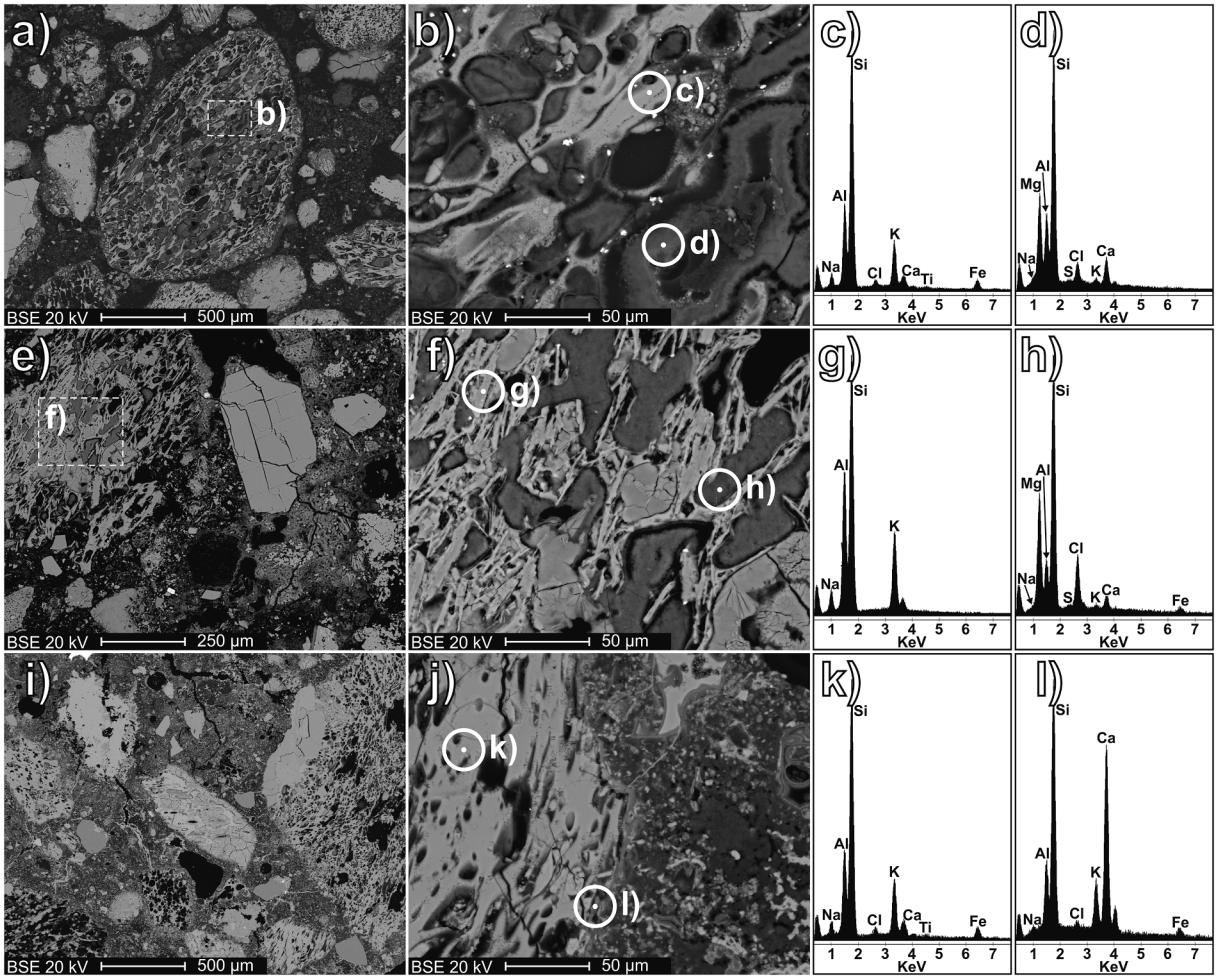

Fig. 8. a, b) Backscattered electron images (BSI) of a pumice particle within sample CAE_K4; c) EDS analysis of a portion of unreacted pumice glass indicated in Fig. 6b; d) EDS analysis of a portion of pseudomorphic reaction product indicated in Fig. 6b; e, f) BSIs of a tuff particle within sample CAE_D3; g) EDS analysis of an unreacted sanidine microlith indicated in Fig. 6f; h) EDS analysis of a portion of pseudomorphic reaction product indicated in Fig. 6f; i, j) BSIs of pumice and tuff particles within sample CAE_B3; k) EDS analysis of a portion of unreacted pumice glass indicated in Fig. 6j; l) EDS analysis of a portion of pseudomorphic reaction product indicated in Fig. 6j.

Groups 1a and 1b, with homogeneous, optically-extinct matrices (Fig. 10m, 10n) rich in silicon and magnesium and low on calcium (Fig. 10o). Again, calcium is mainly accumulated in lumps sized from few micrometers to several millimeters, sometimes with spheroidal shape and increasing calcium contents towards their cores (Fig. 10m, 10n, 10p).

Finally, samples of group 3 present heterogeneous binding matrices (Fig. 10q, 10r). Compact cryptocrystalline areas are dominant, varying from optically extinct to interference colors closer to those of calcite, and constituted of dominant calcium, silicon and magnesium, associated chlorine and traces of sulfur, alkalis and iron (Fig. 10s). Nevertheless, it is possible to observe the occurrence of several portions constituted of acicular microcrystals (Fig. 10r) almost exclusively composed of calcium under EDS analysis (Fig. 10t), and thus identifiable as anthropogenic aragonite [62].

4.3. Spectroscopic characterization

The analysis of the ^{29}Si MAS-SS NMR spectra obtained from binder-concentrated samples of Groups 1 and 2 focused on the interpretation of the chemical shifts in the −60 – −120 ppm range. This interval is crucial for the determination of the degree of condensation of SiO_4 tetrahedra [63]. In the analyzed systems, the paracrystalline aluminosilicate nature of constituents influenced both the resulting chemical shift and the degree of broadening and overlapping of the individual ^{29}Si NMR signals related to the various siloxane building units [63], as testified by the broad ^{29}Si MAS NMR spectra with few characteristic features obtained (Fig. 12a, 12c, 12e, 12 g, 12i). Nevertheless, even though univocal discrimination of single siloxane units (from Q^1 dimers to completely condensed Q^4 building units) was not feasible, the degree of articulation of the overall signal in the analyzed chemical shift range allowed a deconvolution into four well-defined peaks (Table 4), likely ascribable to individual phase constituents, either crystalline or paracrystalline/amorphous, characterized by the simultaneous occurrence of different types of siloxane units: i) **Si_01**, with maximums of distribution between −104.1 and −102.1 ppm; ii) **Si_02**, with maximums of distribution between −95.7 and −94.6 ppm; iii) **Si_03**, with maximums of distribution between −92.8 and −88.1; iv) **Si_04**, with maximums of distribution between −86.0 and −84.2 ppm. Differentiations in the occurrence, relative intensities and broadening of peaks (expressed through the full width at half maximum – FWHM) are observable in the samples of the different Mineralogical Groups. Those of Group 1a (CAE_K2, CAE_K7) present only Si_02 and Si_03 peaks, with comparable broadenings and a relevant prevalence of Si_03. Such peaks are dominant also in Group 1b sample (CAE_K4), with broadenings like those of Group 1a samples and Si_02 present in higher relative intensities. Furthermore, Si_01 peak is also present in residual relative intensities. Group 1c sample (CAE_B3) is characterized by a different arrangement of the overall signal, being

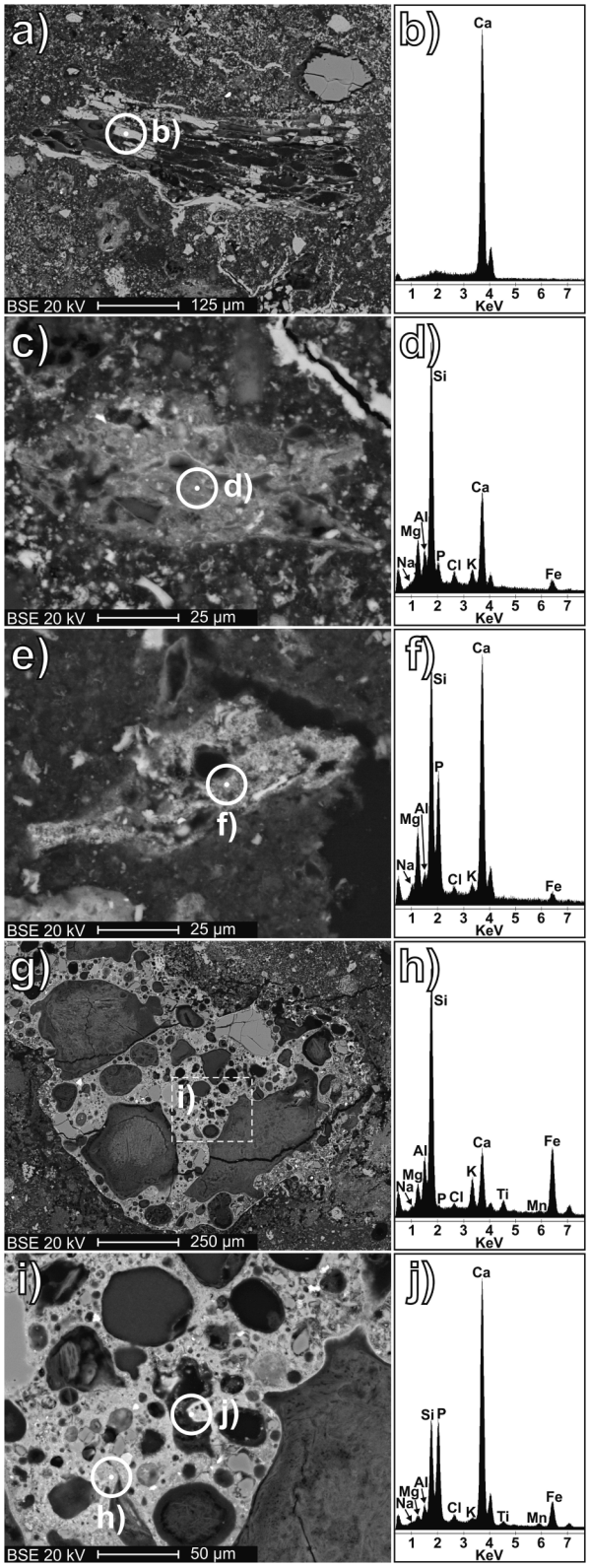

Fig. 9. a) BSI of a charcoal particle within sample CAE_I1; b) EDS analysis of precipitated products indicated in Fig. 7a; c) BSI of an ash cluster within sample CAE_D1; d) EDS analysis of the particle matrix indicated in Fig. 7c; e) BSI of an ash cluster within sample CAE_K1; f) EDS analysis of the particle matrix indicated in Fig. 7e; g, i) BSIs of an ash cluster within sample CAE_B4; h, j) EDS analyses of the particle matrix indicated in Fig. 7i.

dominantly constituted by a Si_02 peak with a FWHM value more than three times higher than the previous samples, associated to a relevant Si_01 peak and a residual Si_04 peak. Si_03 peak is instead absent. Group 2 samples related to the quays are characterized by differentiated ^{29}Si MAS-SS NMR spectra: CAE_I1 presents a signal comparable to those of Group 1a samples (comparable broadenings of the peaks, Si_03 dominant over Si_02), while CAE_D4 is characterized by a dominant Si_02 peak with a broadening comparable to those of Groups 1a and 1b, associated to a narrower Si_03 peak and a residual Si_04 peak. Finally, Group 2 sample related to terrestrial structures (CAE_E2) presents a dominant Si_02 peak, associated to a relevant Si_01 peak and a secondary Si_03 peak.

^{27}Al MAS-SS NMR spectra of the analyzed samples are characterized by the presence of two distinct peaks (Fig. 12b, 12d, 12f, 12 h, 12j). The main one is an asymmetric peak with maximums of distribution within typical chemical shift intervals of tetra-coordinated $^{IV}[Al^{+3}]$ atoms [64]. This region of the spectrum (30 to 90 ppm) has been fitted in the analyzed samples with three peaks (Table 5): i) **Al^{IV}_01**, with maximums of distribution between 61.5 and 65.8 ppm; ii) **Al^{IV}_02**, with maximums of distribution between 51.1 and 57.9 ppm; iii) **Al^{IV}_03**, with maximums of distribution between 40.9 and 46.2 ppm. Furthermore, spectra are characterized by the occurrence of a further asymmetric peak with maximums of distribution within typical chemical shift intervals of Al atoms in hexagonal Al^{VI} coordination [64]. This region of the spectrum (−40 to 20 ppm) has been fitted in the analyzed samples with two peaks (Table 5): i) **Al^{VI}_01**, with maximums of distribution between 3.8 and 9.0 ppm; ii) **Al^{VI}_02**, with maximums of distribution between −5.7 and 1.4 ppm. As observed for the ^{29}Si MAS NMR spectra, differentiations in the obtained signals are evident in the samples of the different Mineralogical Groups. In samples of Group 1a (CAE_K2, CAE_K7), Al^{IV} and Al^{VI} signals are characterized by comparable intensities. Deconvoluted Al^{IV} peaks show comparable relative intensities, with a higher broadening for Al^{IV}_02. As for the deconvoluted Al^{VI} peaks, Al^{VI}_02 is dominant and significantly broader than Al^{VI}_01. Group 1b sample (CAE_K4) shows a higher intensity of Al^{IV} signal. As for the deconvoluted peaks, Al^{IV}_02 is relatively more intense than Al^{IV}_01 in the Al^{IV} region, and Al^{VI}_02 is relatively more intense than Al^{VI}_01 in the Al^{VI} region, while broadenings are comparable with those of Group 1a samples. Group 1c sample (CAE_B3) shows a relevant predominance of Al^{IV} signal, deconvoluted in a main Al^{IV}_02 peak and a broader Al^{IV}_03 peak. The residual Al^{VI} signal has been fitted with a broad Al^{VI}_01 peak. Group 2 samples related to the quays are characterized by differentiated ^{27}Al MAS-SS NMR signals, in accordance with the observations on ^{29}Si MAS-SS NMR spectra. CAE_I1 is characterized by a dominance of Al^{IV} signal, deconvoluted in a broader and slightly more intense Al^{IV}_02 peak, associated to an Al^{IV}_01 one. The Al^{VI} region has been deconvoluted in an Al^{VI}_01 peak and a broad Al^{VI}_02 one, with comparable relative intensities. CAE_D4 is still characterized by a dominance of Al^{IV} signal, deconvoluted in a dominant Al^{IV}_02 peak and a residual narrower Al^{IV}_01 one. The Al^{VI} region has been deconvoluted in a dominant, broad Al^{VI}_02 peak, and a residual Al^{VI}_01 one. Finally, Group 2 sample related to the terrestrial structures (CAE_E2) is characterized by a highly predominant Al^{IV} signal, deconvoluted in a main Al^{IV}_02 peak associated to a Al^{IV}_03 one, both with comparable broadenings, and a residual narrower Al^{IV}_01 peak. The scarce Al^{VI} signal has been fitted with a main Al^{VI}_01 peak and a secondary Al^{VI}_02 one, with comparable broadenings.

The analysis of FTIR spectra obtained from binder-concentrated samples of Groups 1 and 2 focused on the interpretation of the SiO_4 group vibrational bands main peak position, FWHM and asymmetry, and the normalized heights of the $\nu 2$ and $\nu 4$ bands in the CO_3 group (Fig. 13a). These spectroscopic indicators are correlated with the degree of atomic disorder in the crystal structure of silicates and carbonates, respectively [41,54]. I SiO_4/CO_3 peak ratio shows the extent to which silicates are predominant, ranging between 1 and 1.7 and 9–45 in onland structures and underwater concrete samples, respectively (Table 6).

The silicates' main band is associated mainly with asymmetric

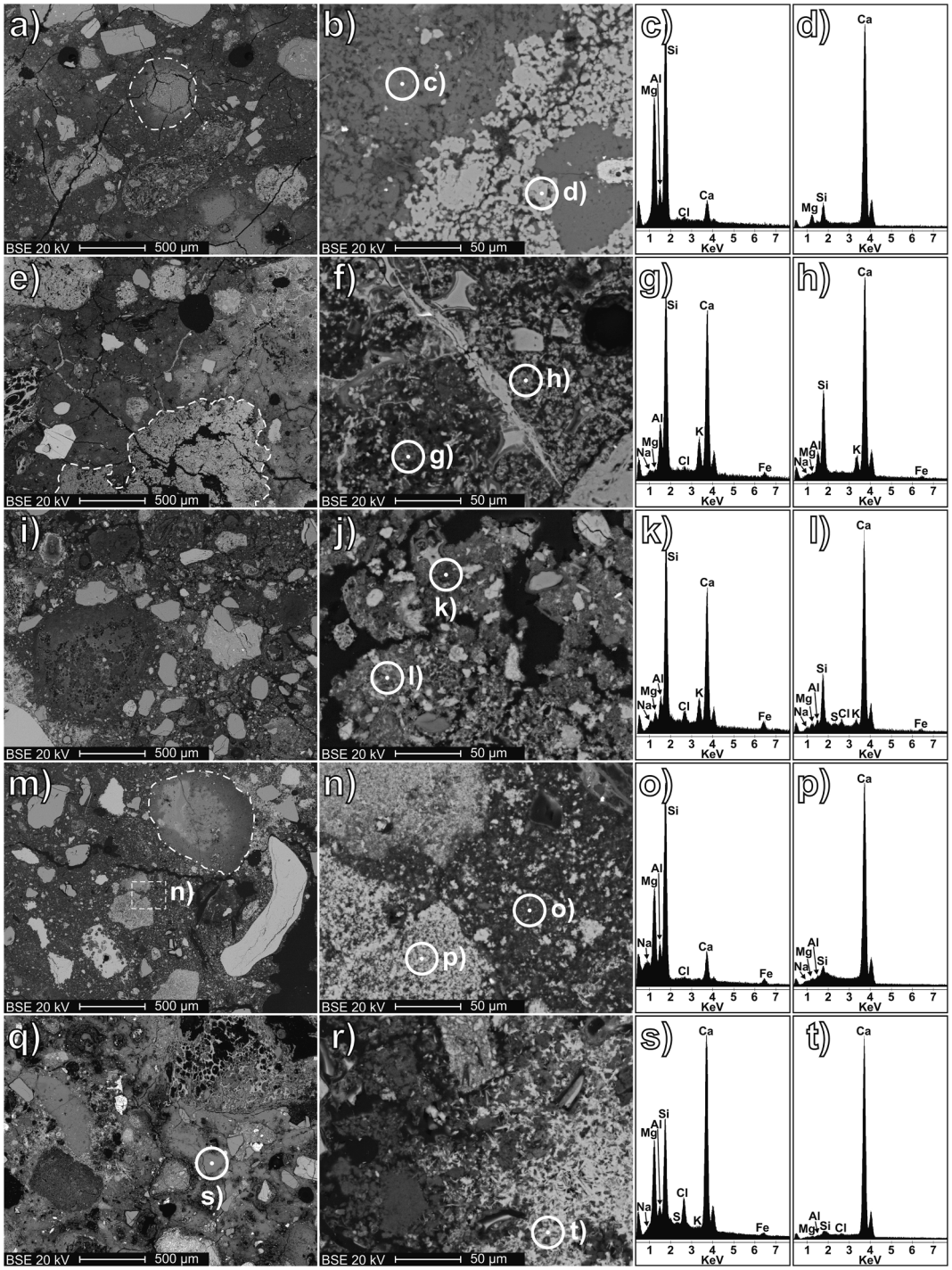

Fig. 10. a) Sample CAE_K7, BSI of the binding matrix (a spheroidal lump with gradient of calcium concentration is highlighted by the dotted hatch line); b) Sample CAE_K2, BSI of an interfacial portion between a lump and the surrounding matrix; c) EDS analysis of a portion of binding matrix indicated in Fig. 8b; d) EDS analysis of a portion of lump indicated in Fig. 8b; e) Sample CAE_B1, BSI of the binding matrix (a lime lump is highlighted by the dashed line); f) Sample CAE_B3, BSI of the binding matrix; g, h) EDS analyses of portions of binding matrix highlighted in Fig. 8f; i, j) Sample CAE_E1, BSI's of the binding matrix; k, l) EDS analyses of portions of binding matrix highlighted in Fig. 8j; m, n) Sample CAE_I1, BSIs of the binding matrix; o) EDS analysis of a portion of binding matrix indicated in Fig. 8n; p) EDS analysis of a portion of lump indicated in Fig. 8n; q) Sample CAE_D5, BSI of the binding matrix; r) Sample CAE_D6, BSI of the binding matrix; s) EDS analysis of a portion of binding matrix indicated in Fig. 8q; t) EDS analysis of a portion of binding matrix highlighted in Fig. 8r.

stretching vibrations of the SiO_4 tetrahedra, between 950 and 1100 cm^{-1}, with a small contribution from the AlO_4 group [65,66]. Deconvolution techniques show limited success in providing significant interpretations of the main silicate peak [67,68], while the main peak position was a robust indicator for the identification of the main phase constituents in the binder-concentrated samples. The peak position in the analyzed samples ranges between 1012 and 1032 cm^{-1} (Table 6), showing a trend towards lower wavenumbers in samples with high amounts of phyllosilicate gels and amorphous fraction below 45 wt% (CAE_K2, CAE_K7, CAE_D4, CAE_I1). Additional silicates vibrational bands are found at 460 and 670 cm^{-1}, characterized as SiO_4 bending modes [69]. Binder-concentrated samples show decreased intensity and

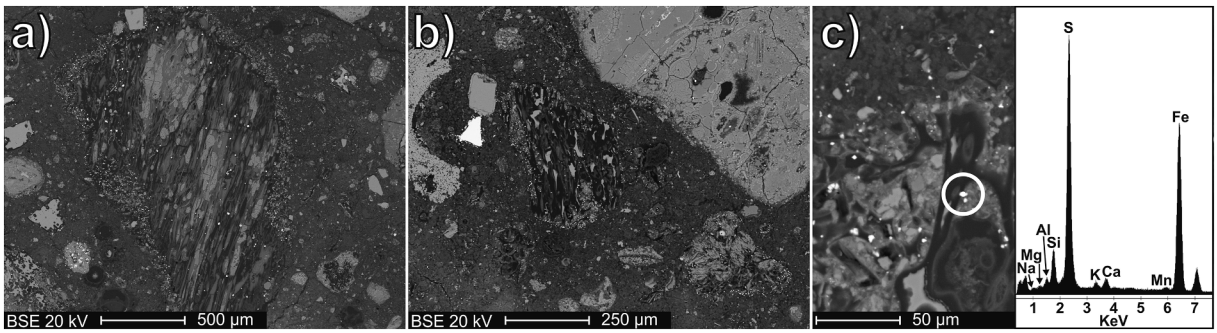

Fig. 11. a, b) Sample CAE_K2, BSIs of pumice and tuff particles with considerable accumulation of euhedral pyrite microcrystals along the interfacial binding matrices, simultaneously showing a noteworthy accumulation of calcium, as indicated by the higher BSE signal; c) sample CAE_K2, BSI showing a detail of the interfacial portion of a pumice particle with relevant pyrite accumulation, and EDS analysis of the indicated particle.

increased width in the 670 cm^{-1} peak, associated with higher atomic disorder.

The FWHM and asymmetry of the SiO_4 group's main vibrational band provide further insight on the degree of atomic disorder in the crystal structure of silicates [41]. In samples CAE_K2, CAE_I1, CAE_K4, CAE_K7, they overlap neatly with several phyllosilicates, including montmorillonites, illite and phlogopite (Fig. 13b). Sample CAE_D4 shows symmetry like the previous samples, with narrower FWHM values shifting towards polymorphs of silica such as cristobalite, quartz and flint (cryptocrystalline quartz). These polymorphs are characterized by a higher degree of atomic order, represented by the narrow FWHM, and higher condensation of their siloxane units with respect to phyllosilicates. Samples CAE_B3 and CAE_E2 show wider FWHM and larger asymmetry, which overlaps with volcanic materials including tuff, pumice, and volcanic ash (*pozzolana*) from Pozzuoli (Naples, Italy). These materials are characterized by highly amorphous glassy materials that are disordered atomically, having the highest degree of condensation of siloxane units.

The spectra of the samples also contain a band at 1630 cm^{-1}, associated with the OH bending vibrations in water, and a pronounced presence of carbonates vibrations bands in on-land and intertidal materials. Carbonates show a main peak in the range 1450–1425 cm^{-1}, and minor peaks at 875 and 713 cm^{-1}, which are associated with the $CO_3(\nu 3)$, $CO_3(\nu 2)$, and $CO_3(\nu 4)$ groups of mineral calcite, respectively [65]. These bands are evidence of the carbonation of the binder, and their atomic disorder is used to assess digenetic processes that alter the chemical structure of the material [70]. The atomic disorder of the calcitic fraction in samples CAE_E2 and CAE_D4 is equivalent to that of modern pyrogenic calcite (above the plaster curve in Fig. 13c), showing that the binder is well preserved. On the other hand, samples CAE_B3 and CAE_I1 are atomically ordered, comparable to geological standards.

The percentage of Total Organic Carbon (TOC) and the stable isotopic composition ($\delta^{13}C$ of organic carbon, $\delta^{13}C$ and $\delta^{18}O$ of carbonates) of binder-concentrated samples from Groups 1 and 2 are reported in Table 7. Results showed differentiations according to the Mineralogical Group of pertinence of the materials. Those of Group 1a (CAE_K2, CAE_K7) are characterized by a fraction of organic carbon around 1 wt %, with an isotopic composition between −27 ‰ and −28 ‰ VPDB. A similar isotopic value was detected for Group 1b sample (CAE_K4), with a slightly lower TOC value. In these samples, due to the reduced amounts of carbonates in the separated fractions a detectable stable isotopic signal could not be obtained. Group 1c sample (CAE_B3) shows the lowest TOC value, with a $\delta^{13}C$ value of −26.6 ‰ VPDB. The carbonate fraction is characterized by a $\delta^{13}C$ value of −13.0 ‰ VPDB and by the highest $\delta^{18}O$ value (−6.3 ‰ VPDB). Group 2 samples from the quays are characterized by the highest amounts of TOC (2 wt%), with isotopic compositions between −26 ‰ and −27 ‰ VPDB, higher than the corresponding underwater samples of Group 1a. Carbonate fractions are characterized by differentiated isotopic compositions, as CAE_I1 sample presents higher $\delta^{13}C$ and $\delta^{18}O$ values (−12.6 ‰ and −8.8 ‰ VPDB, respectively) with respect to those of CAE_D4 (−13.6 ‰ and −10.1 ‰ VPDB, respectively). Finally, Group 2 sample related to terrestrial structures (CAE_E2) has a slightly lower TOC concentration (1.7 wt%) than the underwater samples of the same group, with the lowest $\delta^{13}C$ value amongst the analyzed samples (−25.2 ‰ VPDB). Its carbonate fraction is characterized by the lowest $\delta^{13}C$ value amongst the analyzed samples (−14.5 ‰ VPDB), and by a $\delta^{18}O$ value of −7.5 ‰ VPDB.

5. Discussion

The multi-analytical characterization procedure on the Roman binding composites of Sebastos harbor highlighted the utilization of pozzolanic mixtures based on pure aerial lime, as indicated by the ubiquitous presence of purely calcic lime lumps (Figs. 5, 10) and pozzolanic additives of both natural (Figs. 5, 8) and anthropogenic nature (Figs. 5, 9). Furthermore, aggregate fractions derived from the comminution of shells and grainstone rocks compatible with the local *kurkar* stone outcrops (Figs. 5, 7) were used, in accordance with previous observations in the cores of Sebastos harbor concretes [39].

Based on their compositional characteristics, the analyzed binding composites can be grouped within three different recipes, characterized by peculiar reactional features: i) **Recipe 1** (samples CAE_B1, CAE_B3), constituted by a mix of calcic lime, Phlegraean pozzolan, and *kurkar* stone as *caementa*; ii) **Recipe 2** (samples CAE_K1, CAE_K2, CAE_K3, CAE_K4, CAE_K5, CAE_K6, CAE_K7, CAE_D1, CAE_D2, CAE_D3, CAE_D5, CAE_D6, CAE_D7), constituted by a mix of calcic lime, Phlegraean pozzolan and combustion residues, and *kurkar* stone as *caementa* when used as concrete; iii) **Recipe 3** (CAE_D4, CAE_I1, CAE_I2, CAE_B2, CAE_B4, CAE_E1, CAE_E2, CAE_E3), constituted by a mix of calcic lime, combustion residues, and comminuted *kurkar* stone and shell fragments as fine aggregate.

Concerning the natural pozzolanic additives, analyses showed the occurrence of hypocrystalline pumiceous/tuffaceous ashes and sands (Figs. 5, 8) characterized by mineralogical (Table 2; Fig. 3b), petrographic (Fig. 5a, 5b, 5c) and microstructural/microchemical affinity (Fig. 8) with those within early Imperial binding composites of Roman Vesuvian sites [43,44]. The characteristics of pyroclastic particles are consistent with those observed by [39] in Sebastos harbor concretes. These pozzolanic products are ascribable to the NYT (Neapolitan Yellow Tuff)/post-NYT unconsolidated facies of the Phlegraean fields volcanic activity [71,72], supporting the hypothesis of the Phlegraean provenance of the pozzolanic raw materials of Caesarea Maritima concretes [12,39].

Furthermore, the occurrence of residues from the combustion of organic matter (Fig. 5b, 5d, 5e, 9), besides being potentially related to fuel residues of the lime calcination process, finds ample correspondence with the compositional profiles of several types of binding composites

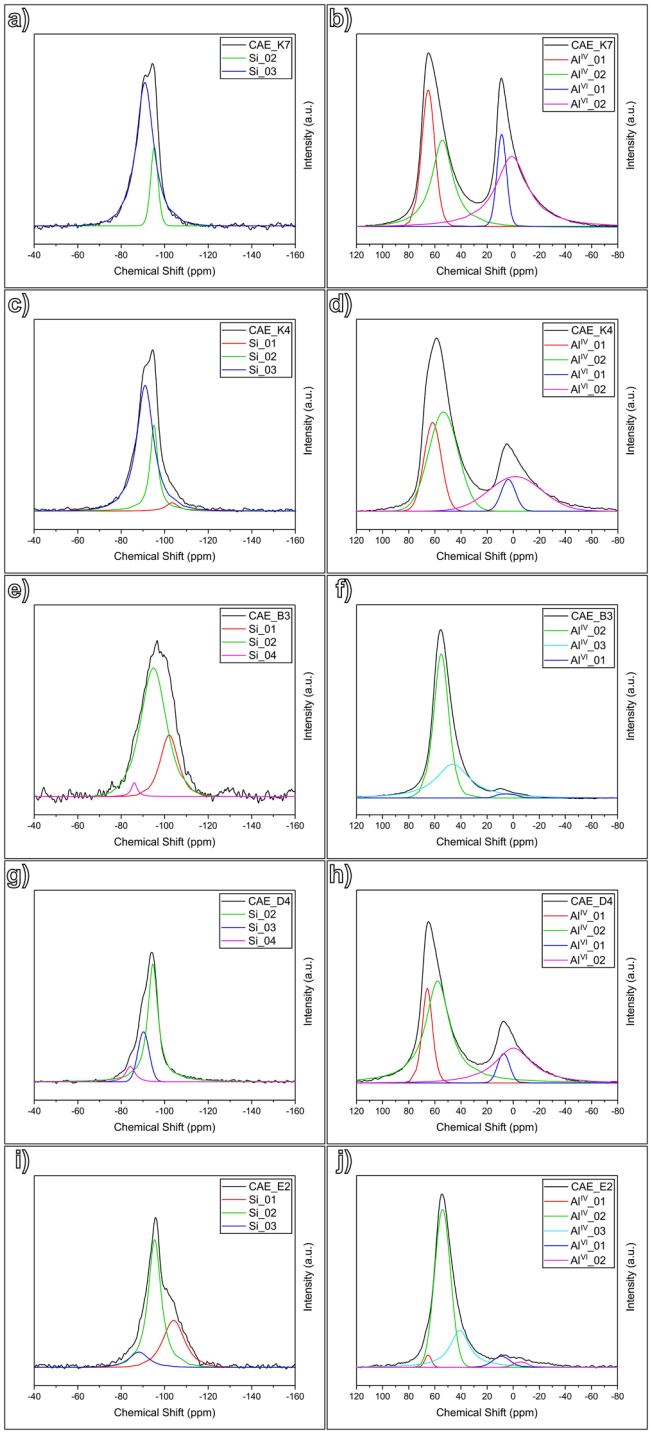

Fig. 12. a, c, e, g, i) ^{29}Si MAS-SS NMR spectra of representative binder-concentrated samples for Groups 1 and 2, reporting the fitted peaks; b, d, f, h, j) ^{27}Al MAS-SS NMR spectra of representative binder-concentrated samples for Groups 1 and 2, reporting the fitted peaks.

from Phoenician-Punic and Roman sites in North Africa, Sardinia and the Levantine regions [17,73,74], especially waterproof linings of hydraulic systems, in which these anthropogenic additives were intentionally added for pozzolanic purposes. The hypothesis of intentional addition is supported at least for Recipe 3, as it contains relevant amounts of the additive not justifiable with inaccurate fuel depuration processes, but it is likely also for Recipe 2, where the lower amounts result in any case higher than the baseline values observable in Recipe 1. The nature of the organic matter from which the combustion residues

Table 4
Results of the fitting procedure on the ^{29}Si MAS-SS NMR spectra of the binder-concentrated samples for Groups 1 and 2. Peak types, relative area fractions, centers of the fitted peaks and their full widths at half maximum (FWHM) are reported.

Sample	Peak type	Area Fraction (%)	Center (ppm)	FWHM (ppm)
CAE_K2	Si_02	25.8	−94.6	4.5
	Si_03	74.2	−90.3	9.7
CAE_K4	Si_01	3.4	−103.4	6.8
	Si_02	25.9	−95.1	4.2
	Si_03	70.7	−91.0	9.2
CAE_K7	Si_02	16.7	−95.2	3.9
	Si_03	83.3	−90.9	9.4
CAE_D4	Si_02	70.2	−94.6	5.6
	Si_03	22.8	−90.2	6.1
	Si_04	7.0	−84.2	5.1
CAE_I1	Si_02	22.2	−95.7	3.7
	Si_03	77.8	−92.8	9.9
CAE_B3	Si_01	24.6	−102.1	9.6
	Si_02	73.1	−94.9	13.9
	Si_04	2.3	−86.0	3.2
CAE_E2	Si_01	31.8	−104.1	11.7
	Si_02	58.6	−95.4	7.0
	Si_03	9.7	−88.1	10.5

Table 5
Results of the fitting procedure on the ^{27}Al MAS-SS NMR spectra of the binder-concentrated samples for Groups 1 and 2. Peak types, relative area fractions, centers of the fitted peaks and their full widths at half maximum (FWHM) are reported.

Sample	Peak type	Area Fraction (%)	Center (ppm)	FWHM (ppm)
CAE_K2	Al^{IV}_01	28.7	64.1	15.7
	Al^{IV}_02	24.0	51.1	22.8
	Al^{VI}_01	14.9	8.3	9.1
	Al^{VI}_02	32.4	1.4	32.1
CAE_K4	Al^{IV}_01	22.8	61.7	15.6
	Al^{IV}_02	43.3	53.4	26.4
	Al^{VI}_01	6.8	3.8	12.9
	Al^{VI}_02	27.1	−1.6	47.4
CAE_K7	Al^{IV}_01	22.5	65.1	11.8
	Al^{IV}_02	29.0	54.3	19.0
	Al^{VI}_01	10.9	8.8	8.7
	Al^{VI}_02	37.6	1.1	29.3
CAE_D4	Al^{IV}_01	16.2	65.8	9.2
	Al^{IV}_02	53.2	57.9	22.1
	Al^{VI}_01	5.5	7.4	10.9
	Al^{VI}_02	25.1	−0.2	33.6
CAE_I1	Al^{IV}_01	30.8	61.5	19.2
	Al^{IV}_02	40.2	52.2	25.8
	Al^{VI}_01	13.8	8.3	15.6
	Al^{VI}_02	15.3	−2.5	50.0
CAE_B3	Al^{IV}_02	58.0	55.0	13.4
	Al^{IV}_03	40.0	46.2	31.2
	Al^{VI}_01	2.0	5.0	18.4
CAE_E2	Al^{IV}_01	2.1	65.1	6.1
	Al^{IV}_02	64.8	54.1	14.4
	Al^{IV}_03	26.1	40.9	17.8
	Al^{VI}_01	5.0	9.0	15.8
	Al^{VI}_02	1.9	−5.7	13.1

are derived can be inferred by the δ^{13}C isotopic composition of the organic residue in the binder-concentrated samples, whose values in-between −25 ‰ VPDB and −28 ‰ VPDB (Table 7) fall within the typical interval for plant species characterized by C3 photosynthetic pathways [75], while they result too low for C4 and CAM plants [76,77]. This is in accordance with the wide availability of C3 plants characterized by abundant levels of soluble silica, particularly fast-growing annual plants such as grasses and cereals like wheat and rye [73], whose seasonal occurrence is common in the Levantine area since prehistorical times despite the arid climate, both as free growing species and cultivated crops [78]. Nevertheless, the low mean annual

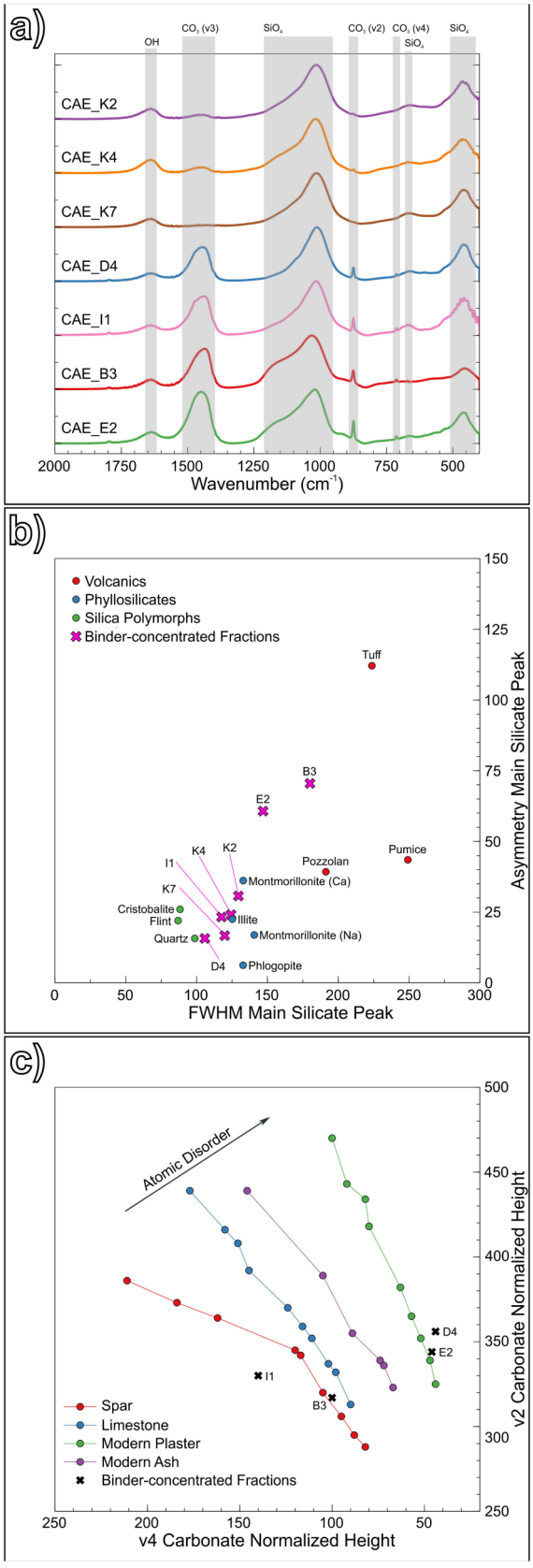

Fig. 13. a) FTIR spectra of representative binder-concentrated samples for Groups 1 and 2 (the main molecular groups are highlighted); b) Main SiO_4 asymmetry and FWHM of silicates standards and binder-concentrated samples, following [41]; c) Grinding curves of calcite following [55], showing the location of binder-concentrated samples.

precipitation (MAP) values of the area would imply a shift of the $\delta^{13}C$ toward slightly higher values with respect to those observed in the analyzed samples [75,79], thus suggesting at least a partial occurrence of combustion residues of different origins. In this perspective, several studies [17,73,74] suggested the utilization of ashes derived from the combustion of manure produced by herbivore animals (cow, horse, sheep) as additives in ancient pozzolanic binders, commonly rich in amorphous, mainly aluminosilicate compounds [80] and thus showing good pozzolanic reactivity in alkaline, Ca-saturated solutions [73]. The occurrence of at least partial fractions of animal ashes in the analyzed materials is confirmed both by the systematic presence of reduced aliquots of calcium phosphates in the ash particles (Fig. 9) and by the detection of traces of hydroxyapatite (Table 3) in the binder-concentrated samples with higher total organic carbon (CAE_D4, CAE_I1, CAE_E2).

Recipe 1 (corresponding to Mineralogical Group 1c) was employed to produce the concretes constituting the vaults of the storehouses along the coastline in front of the harbor structures. In the overall balance between the competitive carbonation and hydration process of pozzolanic systems [81], these materials show a prevalence of the latter, as demonstrated by the XRPD ratios between anthropogenic carbonates and paracrystalline compounds (Tables 2, 3), ascribable to pozzolanic reaction products such as C–S–H and C–A–H phases, commonly characterized by the absence of crystal-like long-range ordering [1]. This is also demonstrated by the silicate/carbonate ratio determined by FTIR (Table 6). Nevertheless, the impact of carbonation is considerable, and this is consistent with the availability of atmospheric CO_2 during the setting of on-land concretes. Concerning the degree of atomic order of constituting carbonates measured by FTIR, a disordered calcitic fraction, typical for anthropogenic carbonates, should be expected. Nevertheless, the atomic structure is surprisingly comparable to the atomic disorder of spar (Fig. 13c). The interaction between the metastable hydrated products and the disordered calcite may have promoted internal recrystallization. This recrystallization process was observed previously in mortars with pyroclastic aggregates, in which a correlation was found between the hydraulicity of the material and the increased atomic order in the calcitic fraction of the binder [41]. This hypothesis is further corroborated by the microstructural evidence of carbonates precipitation within the capillary porosity of the analyzed materials (Fig. 10e, 10f), and by the $\delta^{13}C$ and $\delta^{18}O$ values of carbonates (Table 7), significantly diverging from the ideal values of unaltered and uncontaminated anthropogenic carbonates within binding materials [82,83]. The occurrence of pozzolanic phases is confirmed by the microstructural and microchemical characteristics of the binding matrices (Fig. 10e, 10f, 10 g, 10 h), yet the mineralogical analyses did not provide relevant information on their compositional and structural characteristics, as the XRPD pattern of the binder-concentrated sample is solely characterized by a relevant hump centered around 33 [°2θ] (Fig. 4), without diffraction reflexes ascribable to C–S–H and C–A–H phases. This is an indication of the paracrystalline to amorphous nature of the hydrated phases formed through pozzolanic reaction processes. This lack of information was compensated through spectroscopic analyses, which resulted highly informative in determining the nature and short-range ordering of anthropogenic aluminosilicate constituents. In the interpretation of the NMR data, the possible contribution of aggregate-related mineral phases to the overall NMR signal was considered negligible, due to their limited occurrence in the binder-concentrated samples determined by XRPD-QPA. ^{29}Si MAS-SS NMR spectrum deconvolution (Table 4; Fig. 12e) highlighted the occurrence of a residual narrow Si_04 peak with typical ppm values for Q^2 siloxane chains of conventional C–S–H phases with inosilicate structures ascribable to tobermorite-jennite solid solutions [84], together with a more relevant broad Si_01 peak close to typical ppm values for completely condensed Q^4 siloxane building units of the distorted tetrahedral network of silicate glasses, indicating a residual permanence of unreacted pozzolanic additives. Nevertheless, the most relevant contribution is ascribable to the Si_02 peak, characterized by

Table 6
Molecular vibrational modes analysis of selected binder-concentrated samples for Groups 1 and 2, obtained by peak shape quantification of FTIR spectra. Silicate main peak position, full widths at half maximum (FWHM) and asymmetry are reported, as well as the carbonate $\nu4$ and $\nu2$ normalized heights, and the silicate/carbonate ratio.

Sample	Silicate main peak position (cm^{-1})	Silicate main peak asymmetry	Silicate main peak FWHM	Carbonate $\nu4$ Normalized	Carbonate $\nu2$ Normalized	Silicate/carbonate ratio
CAE_K2	1013	31	130	–	–	19.4
CAE_K4	1019	24	124	–	–	9.2
CAE_K7	1016	17	120	–	–	45.7
CAE_D4	1012	16	106	44	356	1.6
CAE_I1	1015	23	118	140	330	1.4
CAE_B3	1032	70	180	100	317	1.3
CAE_E2	1020	61	147	46	344	1.0

Table 7
Total Organic Carbon (TOC) and stable isotopic composition of carbon ($\delta^{13}C$) of selected binder-concentrated samples for Groups 1 and 2.

Sample	TOC (wt.%)	$\delta^{13}C$ Organic Carbon (‰)	$\delta^{13}C$ Carbonates (‰)	$\delta^{18}O$ Carbonates (‰)
CAE_K2	0.9	−27.28	–	–
CAE_K4	0.7	−27.21	–	–
CAE_K7	1.1	−27.94	–	–
CAE_D4	2.0	−26.01	−13.57	−10.12
CAE_I1	2.0	−26.55	−12.64	−8.81
CAE_B3	0.6	−26.58	−12.99	−6.31
CAE_E2	1.7	−25.23	−14.51	−7.5

ppm values in-between Q^2 siloxane chains and Q^3 siloxane sheets and wide FWHM indicative of reduced structural order [63]. This indicates that the main hydrated calcium silicate constituting the pozzolanic network of these binding composites is likely a poorly crystalline C–S–H phase with a hybrid ino- and phyllosilicate structure of the okenite/nekoite type [85,86], typically precipitating in Ca-deficient cementitious systems [87]. This is justifiable by the partial sequestration of free Ca due to the carbonation process, decreasing the amount of available Ca for the pozzolanic reaction. The interpretation of the ^{27}Al MAS-SS NMR signal (Table 5; Fig. 12f) gave further insights on the structural characteristics of the pozzolanic phases. The most relevant contribution of the Al^{IV}_02 peak is ascribable to a fraction of tetrahedral Al isomorphically substituting Si in the structure of hydrated calcium silicates, indicating the C–A–S–H nature of the phases. This is in accordance with observations on the concrete samples of Sebastos harbor analyzed during the ROMACONS project [39]. Furthermore, the Al^{IV}_03 peak is ascribable to the Al in the distorted tetrahedral networks of unreacted pozzolanic additives, while the residual Al^{VI}_01 peak is ascribable to Al atoms in the octahedral sites of paracrystalline C–A–H phases [88]. The reduced intensity of this last contribution indicates that the formation of hydrated calcium aluminates is not favored in these pozzolanic systems, with preferential incorporation of Al in the structure of C–A–S–H phases. The MAS-SS NMR data are further corroborated by the FTIR results (Table 6; Fig. 13a, 13b). A shift to lower wavenumbers in the main SiO_4 peak position is correlated with an increase in the ratio of Al/Si in aluminosilicate gels [66,89], while the decreased intensity and increased width of the additional silicates vibrational bands are associated with decreased polymerization and structural order [90], further confirmed by the wide FWHM and large asymmetry of the SiO_4 group main vibrational band.

Recipe 2 was employed to produce the underwater concrete blocks of the moles and the infill concrete of the internal quays in the intermediate harbor, where it was also used as a mortar in-between the ashlars of the topmost belt. Concrete samples, clustered within Mineralogical Groups 1a and 1b (Fig. 3a), show a significant prevalence of pozzolanic reaction over aerial reaction, as indicated by the silicate/carbonate ratio determined by FTIR (Table 6) and by the reduced amount of carbonate phases in the binder-concentrated samples (Table 3). This is in accordance with the limited availability of atmospheric CO_2 during the setting process of underwater binding composites. Nevertheless, the bulk mineralogical assemblage (Table 2) is characterized by a moderate occurrence of calcite, not completely justifiable with the subordinate *kurkar* fine aggregate fraction and with the carbonate component of the ash from combustion residues, thus indicating a certain impact of the carbonation process in the binding fraction composition of the analyzed materials. This is testified by petrographic and microstructural analyses, showing a preferential accumulation of anthropogenic carbonates within compact lumps (Fig. 5a, 10a, 10b), likely separated by sedimentation during the preparation of the binder-concentrated samples. Such inhomogeneous distribution may be related to poor manufacturing of the lime binder, either in the calcination phase (permanence of residual uncalcined cores of the raw materials) or during the slaking and mixing process. It could also indicate the employment of a hot-lime mixing technology [91], inducing a characteristic enrichment of macroscopic lime lumps [92]. Furthermore, these peculiar textural features may be influenced by the chemical and biological factors of the reactive environment, leading to anomalous carbonation rates during the first setting phases of the binding composites. Indeed, they could be related to the employment of marine saltwater in the mixing process, as suggested by the systematic occurrence of halite in the bulk mineralogical profiles (Table 2) and chlorine in the binding matrices (Fig. 10c). High chloride concentrations in lime-saturated solutions are promoting flocculation of portlandite particles, due to the lowering of the zeta potential induced by the physical adsorption of chloride on crystal surfaces [93]. Furthermore, the influence of high NaCl concentrations in increasing portlandite solubility is demonstrated [94]. The combined effect of increased portlandite flocculation and dissolution may be relevant in binding mixtures employing relevant amounts of saltwater, especially in shallow, closed seas such as the Mediterranean, characterized by considerable mean salinity increases in the areas facing the Levantine regions with respect to the values attested in the western areas and around the Italian peninsula [95]. This is a potential trigger for the rapid carbonation of lime even without considerable uptake of atmospheric CO_2, provided that an alternative source of carbonate is available in solution. In this perspective, concrete samples showed the occurrence of euhedral pyrite microcrystals (Fig. 11), preferentially accumulated in portions characterized by pronounced carbonation, whose origin may be ascribed to biotic processes related to the trophic activity of sulphate-reducing bacteria [96]). Such microorganisms are common in anoxic marine sediments, and they perform anaerobic respiration through the reduction of marine sulphates, counterbalanced by the oxidation of organic matter [97]. Their proliferation in the analyzed materials may have been favored by the wide availability of organic matter, both from the combustion residues in the binding mixtures and from the disposable timber formworks. The oxidation of organics to soluble bicarbonate may have led to a considerable carbonation of the lime binder, no longer available for the pozzolanic reaction. This is confirmed both by the absence of crystalline Ca-based pozzolanic products in the XRPD patterns of the binder-concentrated samples (Table 3) and by the low calcium amounts in the binding matrices (Fig. 10b, 10c). Nevertheless, a

pronounced dissolution of the pozzolanic additives is observable (Fig. 5a, 5b, 8a, 8b, 8e, 8f, 9c, 9e), likely favored by saltwater, increasing dissolution of silicates due to the pH increase promoted by the formation of sodium hydroxide after the interaction between calcium hydroxide and sodium chloride [98,99]. In the analyzed pozzolanic systems, the paucity of soluble calcium led to alternative routes of reaction of the soluble silica, precipitating abundant paracrystalline, Mg-based phyllosilicate gels (Tables 2, 3; Fig. 3b, 4). The diffractometric contributions of these compounds are limited to few asymmetric broad maxima of low diffracted intensity, typical for lamellar and turbostratic structures with nanometer-sized coherent scattering domains [100]. Furthermore, they present marked similarities with those of magnesium-silicate-hydrate (M–S–H) phases formed in modern high Mg Portland-based blend cements [101], and recently attested in Mg-rich ancient pozzolanic binders [17,102]. In accordance with previous literature data [17], discrepancies with the diffractometric patterns of reference 2:1 talc-like M–S–H structures [103] may be attributed to the incorporation of Al within the crystal structure, suggesting the occurrence of a M–A–S–H gel with a saponite-like structure. This is supported by the observed Al enrichments in the binder matrices (Fig. 10c). Additional structural information on pozzolanic precipitates was obtained through spectroscopic analyses. ^{29}Si MAS-SS NMR spectra (Table 4; Fig. 12a, 12c) are showing a significant prevalence of the Si_03 contribution, ascribable to the spectroscopic signal of M–A–S–H gels. Its ppm values in-between Q^2 siloxane chains and Q^3 siloxane sheets are only apparently contradictory for phyllosilicate-like structures, due to their nanocrystalline characteristics implying relevant truncation of the Q^3 silica sheets, with consequent increase of the edge sites density [17,103]. Furthermore, the analyzed materials present a secondary Si_02 contribution, indicating the occurrence of Ca-deficient hybrid ino-phyllosilicate C–A–S–H phases, and CAE_K4 presents a residual Si_01 contribution, ascribable to a fraction of unreacted pozzolan. ^{27}Al MAS-SS NMR spectra (Table 5; Fig. 12b, 12d) are characterized by two contributions in the region of tetracoordinated aluminum: i) Al^{IV}_02, ascribable to the tetrahedral Al in the structure of C–A–S–H phases; ii) Al^{IV}_01, at higher ppm values, ascribable to the tetrahedral Al in the structure of M–A–S–H phases. Two contributions are also detectable in the region of hexacoordinated aluminum: i) Al^{VI}_01, ascribable to the Al atoms in the octahedral sites of paracrystalline C–A–H phases; ii) Al^{VI}_02, at lower ppm values, ascribable to Al atoms in the octahedral sites of M–A–S–H phases, indicating a partial dioctahedral nature of the anthropogenic phyllosilicate gels. MAS-SS NMR data are further corroborated by the FTIR results (Table 6; Fig. 13a, 13b). The presence of M–A–S–H gels influences spectral shapes in terms of shift, asymmetry and FWHM reduction of the SiO_4 group main vibrational band with respect to the sample for Recipe 1: such features are related both to the different crystallographic arrangement of the dominant pozzolanic phases, and to their higher degree of structural order. The abundant precipitation of M–A–S–H phases in the analyzed materials may be justified by several sources of soluble magnesium in the employed recipe: i) the seawater, with a concentration of magnesium ions up to 3.7 wt% in the overall amount of soluble salts [104]; ii) theashcomponent of the combustion residues, characterized by relevant amounts of magnesium (Fig. 9d, 9f), typical for animal ashes [80]; iii) the *kurkar* aggregate fraction, rich in magnesian calcite (Fig. 6b). Magnesium may have leached from the silicate framework of the combustion residues after dissolution through pozzolanic processes, while its release from the sandstone aggregate may be related to the destabilization of its magnesian component, likely triggered by dedolomitization processes promoted by an alkali-carbonate reaction [105], whose incidence in the analyzed pozzolanic systems is justifiable by the occurrence of relevant sources of alkalis, i.e. the saltwater and the K-rich aluminosilicate glass of the pumice particles. The abundant availability of soluble magnesium also influenced the carbonation processes of the mortars in-between the ashlars of the topmost belt, where aerial setting resulted more relevant with respect to concretes due to the greater exposure to atmospheric CO_2, as indicated by the abundance of anthropogenic carbonates in the bulk samples (Table 2), reflected by the separate clustering in the PCA plot (Mineralogical Group 3, Fig. 3a). In these samples, the relevant occurrence of the metastable calcium carbonate polymorph aragonite (Table 2; Fig. 10r, 10 t) may be related to the stabilizing effect of Mg ions, hindering its conversion into the stable polymorph calcite by incorporation into the crystal structure of the phase [106]. High Mg activity may have also favored the precipitation of magnesian carbonates, such as magnesian calcite and structurally disordered dolomite (Table 2; Fig. 3b), whose occurrence in magnesian binding systems is generally not favored [107], but it was experimentally precipitated at low temperature by the microbial mediation of sulphate-reducing bacteria [108].

Recipe 3 (corresponding to Mineralogical Group 2) was employed as bedding mortar both on-land, in the external masonry leaves of the vaulted storehouses and in-between the ashlars of the Temple of Roma and Augustus, and in underwater/intertidal portions, in the external masonry leaves of the internal quays and as floor bedding in the inner harbor. Such differentiated employment influenced the balance between aerial and pozzolanic reactions in the binding systems, as indicated by the differentiated silicate/carbonate ratios determined by FTIR (Table 6): in accordance with the availability of atmospheric CO_2, underwater/intertidal samples (CAE_I1, CAE_D4) are showing a prevalence of the silicate signal, while a more balanced ratio is observable for the sample related to the on-land mortar (CAE_E2). Nevertheless, materials in contact with water are showing greater degrees of carbonation with respect to those observed in samples related to Recipe 2, even when placed in fully water-saturated environments such as those of floor beddings. Such evidence may be related to the utilization of the sole combustion residues as pozzolanic additive, replacing the natural pozzolan with less reactive sandstone aggregate, with consequent reduction of Si activity in pore solution. The degree of atomic order of carbonates measured by FTIR (Fig. 13c) gave interesting insights on the differentiated crystallinity of the phases according to the precipitation environment: in the on-land and intertidal samples (CAE_E2, CAE_D4) it is equivalent to that of pyrogenic calcite, indicating good preservation of the binder, while in the underwater material (CAE_I1) it is comparable to that of geologic standards, suggesting recrystallization of the carbonate binder mediated by the pozzolanic environment, as observed for Recipe 1 samples. An alternative hypothesis to justify this peculiar analytical evidence should consider the influence of bacterial-mediated precipitation in promoting a higher degree of structural order of carbonates, as this sample is showing the same microstructural features observed for Recipe 2, indicating the action of sulphate-reducing bacteria. δ^{13}C and δ^{18}O values of carbonates (Table 7) are consistent with the FTIR observations, with values closer to those of unaltered and uncontaminated anthropogenic carbonates [82,83] for samples CAE_D4 and CAE_E2, characterized by a lower degree of structural order. The diversified precipitating environment impacted also on the compositional and structural characteristics of pozzolanic phases. XRPD patterns (Tables 2, 3; Fig. 3b, 4) are devoid of diffraction reflexes ascribable to C–S–H and C–A–H phases, apart from the occurrence of limited aliquots of carboaluminate AFm phase in CAE_I1 sample, highlighting the paracrystalline to amorphous nature of the Ca-based pozzolanic compounds. On the other hand, underwater/intertidal materials are characterized by the occurrence of significant amounts of M–(A)–S–H phases (Tables 2, 3; Fig. 3b, 4), structured also in the form of crystalline lizardite in CAE_I1 sample, while they are present in low to null amounts in on-land binding composites. This is an indication of the relevant impact of seawater in favoring the precipitation of magnesian aluminosilicates, not only through the increased dissolution of pozzolanic additives promoted by pH increase, but also by alkali-carbonate reaction of magnesian carbonates, both in the *kurkar* aggregate and shell fragments. High Mg activity, likely in combination with trophic processes of sulphate-reducing bacteria, may have induced the precipitation of structurally disordered dolomite, detected in CAE_I1 sample (Table 2). Mineralogical evidence was reinforced by the interpretation of MAS-SS

NMR results (Tables 4, 5; Fig. 12g, 12 h, 12i, 12j). The outcomes are the following: i) relevant Si_01 and Al^{IV}_03 peaks were detected in on-land CAE_E2 sample, ascribable to the unreacted pozzolanic additive: this confirms the lower pozzolanic reactivity of terrestrial materials; ii) all samples present relevant Si_02 and Al^{IV}_02 peaks ascribable to Ca-deficient hybrid ino-phyllosilicate C–A–S–H phases, confirming their preferential formation over conventional C–S–H phases with inosilicate structures (identified by the Si_04 peak in the sole CAE_D4 sample) and C–A–H phases (identified by the Al^{VI}_01 peak); iii) spectroscopic contributions of M–A–S–H phases (Si_03, Al^{IV}_01 and Al^{VI}_02 peaks) are dominant in the underwater CAE_I1 sample, subordinate in the intertidal CAE_D4 sample, and residual in the on-land CAE_E2 sample: this further confirms the influence of saltwater in the precipitation of these anthropogenic compounds. NMR data are further corroborated by FTIR results (Fig. 13a, 13b; Table 6): on-land sample CAE_E2 is characterized by a higher wavenumber position of the SiO_4 group main vibrational band with respect to those of underwater/intertidal samples, with a higher asymmetry and FWHM. This is consistent with a prevalence of highly disordered C–A–S–H phases over more structurally ordered M–A–S–H gels.

6. Conclusions

Characterization studies on the binding composites employed for the construction of the Roman harbor of Sebastos in Caesarea Maritima highlighted their complex composition and reactional framework, shedding new light on the technological skills reached by Roman builders in optimizing the strength and durability of complex structures through the careful formulation of building materials. Furthermore, a better understanding of the crystal-chemical characteristics of ancient pozzolanic materials was gained, through a comprehensive characterization of anthropogenic binding products at different degrees of structural order. This was possible thanks to an integrated analytical protocol entailing both conventional mineralogical-petrographic-microstructural approaches and in-detail spectroscopic studies, with relevant implications for the understanding of the cohesive behavior of complex cement-free alternative binders.

In the analyzed samples, the adoption of three different recipes appears related both to the optimization of the supply of raw materials and to intentional technological choices, to properly stimulate reactive processes according to the characteristics of the precipitating environment.

On-land constructions show an accurate utilization of the precious imported Phlegraean pozzolan, exclusively used in the structural concrete casts of the vaulted storehouses. In all remaining on-land building contexts, it was replaced with a locally available artificial pozzolanic additive mainly constituted by combustion residues of organic materials, likely a mixture of charred remains of grasses, wheat, rye and manure by herbivore animals. The utilization of this peculiar pozzolanic additive is of particular interest, being ascribable to Phoenician-Punic building practices [17,73]: this is an indication of the technological crossover in the construction site of Caesarea Maritima, still highly influenced by the traditions of the populations controlling the area before the Roman conquest. Despite the marked pozzolanic character of on-land binding composites, reaction features showed a relevant carbonation of the employed lime-based binder, in accordance with the wide availability of atmospheric CO_2 in terrestrial contexts. As for the detected pozzolanic phases, preferential precipitation of structurally disordered C–A–S–H phases with Ca-deficient hybrid ino-phyllosilicate structures was observed in lieu of conventional assemblages of C–S–H phases with inosilicate structures [18] and C–A–H phases in layered octahedral coordination [88]: this peculiar feature, consistent with recent observations on Roman pozzolanic concretes in terrestrial contexts [109], may be ascribed to reduced availability of free lime during the pozzolanic reaction stages, sequestrated by the competitive carbonation process [81].

The selective utilization of the Phlegraean pozzolan only for concrete production is observable also in underwater and intertidal contexts, in association with the artificial pozzolan based on combustion residues. The combined utilization of different pozzolanic additives likely influenced the peculiar pozzolanic reactive pathways observed in this constructional context. More in detail, marked sequestration of soluble Ca was observed, mainly concentrated in carbonated lumps. This process, besides being potentially related to poor manufacturing procedures or hot-lime mixing, may have been triggered by considerable flocculation and dissolution of portlandite promoted by high water salinity, and by subsequent anaerobic bacterial-mediated carbonation. These factors caused a divergence of the pozzolanic reactive systems from the conventional Si/Al/Ca stability fields, leading to significant precipitation of M–A–S–H phases due to the occurrence of soluble Mg in pore solution, related to its availability in seawater and to its release not only from Mg-rich combustion residues, but also from *kurkar* aggregates and shell fragments after alkali-carbonate reaction. Furthermore, high Mg activity may have been crucial for the precipitation of unconventional calcic-magnesian anthropogenic carbonates (magnesian calcite and structurally disordered dolomite) in binding materials more exposed to the environmental atmosphere, likely with a relevant contribution of bacterial activity. The precipitation of M–A–S–H gels was fundamental to guarantee proper cohesion to the binding composites, compensating the paucity of C–A–S–H/C–A–H phases related to the deficit of soluble Ca available for conventional, Ca-based pozzolanic reactions. In this perspective, it is possible to hypothesize a deliberate modification of the mix design of maritime concretes by the addition of the artificial pozzolanic additive, possibly after the first constructional phases of the underwater structures, to compensate for their poorer early-setting properties with respect to their terrestrial counterparts.

As a general conclusive remark, the articulated compositional framework of the analyzed materials highlighted the complex reactive pathways of ancient pozzolanic binders, highly influenced by chemical-physical conditions of the precipitating environments. This is a demonstration of the advanced skills of ancient builders in managing materials composition and properties, to satisfy the necessary building requirements.

CRediT authorship contribution statement

Michele Secco: Conceptualization, Data curation, Formal analysis, Funding acquisition, Investigation, Methodology, Project administration, Writing – original draft, Writing – review & editing. **Yotam Asscher:** Conceptualization, Data curation, Formal analysis, Funding acquisition, Investigation, Methodology, Project administration, Writing – original draft, Writing – review & editing. **Giulia Ricci:** Conceptualization, Data curation, Formal analysis, Investigation, Methodology, Writing – review & editing. **Sergio Tamburini:** Data curation, Formal analysis, Writing – review & editing. **Nereo Preto:** Data curation, Formal analysis, Writing – review & editing. **Jacob Sharvit:** Conceptualization, Funding acquisition, Supervision, Writing – review & editing. **Gilberto Artioli:** Conceptualization, Funding acquisition, Methodology, Project administration, Supervision, Writing – review & editing.

Declaration of Competing Interest

The authors declare that they have no known competing financial interests or personal relationships that could have appeared to influence the work reported in this paper.

Data availability

Data will be made available on request.

Acknowledgements

The project was carried out in the frame of the research agreement between the CIRCe center of the University of Padova and the IAA. The IAA personnel, especially archaeologists Peter Gendelman and Uzi 'Ad, is gratefully acknowledged for their support during the field work. The webmasters of the site www.biblewalks.com are gratefully acknowledged for providing permission to use the aerial photos of the Caesarea Maritima site reported in Fig. 1. The research project received partial financial support from the University of Padova, in the frame of the project "Archaeometric investigations on the Euganean Pozzolan" (principal investigator: Dr. Michele Secco, BIRD 2020 of the Department of Cultural Heritage, project code: SECC_BIRD20_01). Francesca Andolfo is gratefully acknowledged for revising the English text.

Appendix A. Supplementary data

Supplementary data to this article can be found online at https://doi.org/10.1016/j.conbuildmat.2022.129128.

References

[1] F. Massazza, Properties and applications of natural pozzolanas, in: J. Bensted, P. Barnes (Eds.), Structure and Performance of Cements, Spon Press, London, 2002, pp. 326–352.
[2] Artioli, G., Secco, M., Addis, A., 2019. The Vitruvian legacy: mortars and binders before and after the Roman world, in: Artioli, G., Oberti, R. (Eds.), EMU Notes in Mineralogy, Vol. 20: The Contribution of Mineralogy to Cultural Heritage. European Mineralogical Union, London, pp. 151-202.
[3] B. Lothenbach, K. Scrivener, R.D. Hooton, Supplementary cementitious materials, Cem. Concr. Res. 41 (2011) 1244–1256.
[4] R. Snellings, G. Mertens, J. Elsen, Supplementary cementitious materials, Rev. Mineral. Geochem. 74 (1) (2012) 211–278.
[5] A. Hauptmann, Ü. Yalcin, Lime plaster, cement and the first puzzolanic reaction, Paleorient 26 (2) (2000) 61–68.
[6] M. Secco, L. Valentini, A. Addis, Ancient and modern binders: naturally nanostructured materials, in: G. Lazzara, R. Fakhrullin (Eds.), Nanotechnologies and Nanomaterials for Diagnostic, Conservation and Restoration of Cultural Heritage, Elsevier, Amsterdam, 2019, pp. 205–237.
[7] M. Theodoridou, I. Ioannou, M. Philokyprou, New evidence of early use of artificial pozzolanic material in mortars, J. Archaeol. Sci. 40 (8) (2013) 3263–3269.
[8] A.V. Greco, *Virtutes materiae*. Il contributo delle fonti latine nello studio di malte, intonaci e rivestimenti nel mondo romano, Nuove Grafiche Puddu, Cagliari, 2011.
[9] M. Mogetta, A new date for concrete in Rome, The Journal of Roman Studies 105 (2015) 1–40.
[10] M. Mogetta, The Origins of Concrete Construction in Roman Architecture, Technology and Society in Republican Italy, Cambridge University Press, Cambridge, 2021.
[11] M.P. Vitruvio, De Architectura, Einaudi, Torino, 1997.
[12] M.D. Jackson, Sea-water concretes and their material characteristics, in: J. P. Oleson (Ed.), Building for Eternity, Oxbow Books, Philadelphia, 2014, pp. 141–188.
[13] F. Marra, E. D'Ambrosio, M. Gaeta, M. Mattei, Petrochemical identification and insights on chronological employment of the volcanic aggregates used in ancient Roman mortars, Archaeometry 58 (2016) 177–200.
[14] C. Brandon, R.L. Hohlfelder, J.P. Oleson, C. Stern, The roman maritime concrete study (ROMACONS): the harbour of chersonisos in crete and its italian connection, J. Mediterr. Geography 104 (2005) 25–29.
[15] J.P. Oleson, L. Bottalico, C. Brandon, R. Cucitore, E. Gotti, R.L. Hohlfelder, Reproducing a roman maritime structure with vitruvian pozzolanic concrete, J. Roman Archaeology 19 (2006) 31–52.
[16] C.J. Brandon, R.L. Hohlfelder, M.D. Jackson, J.P. Oleson, Building for eternity: the history and technology of Roman concrete engineering in the sea, Oxbow Books, Philadelphia, 2014.
[17] M. Secco, S. Dilaria, J. Bonetto, A. Addis, S. Tamburini, N. Preto, G. Ricci, G. Artioli, Technological transfers in the Mediterranean on the verge of Romanization: Insights from the waterproofing renders of Nora (Sardinia, Italy), J. Cult. Heritage 44 (2020) 63–82.
[18] I.G. Richardson, The nature of CSH in hardened cements, Cem. Concr. Res. 29 (1999) 1131–1147.
[19] I.G. Richardson, Tobermorite/jennite-and tobermorite/calcium hydroxide-based models for the structure of CSH: applicability to hardened pastes of tricalcium silicate, b-dicalcium silicate, Portland cement, and blends of Portland cement with blast-furnace slag, metakaolin, or silica fume, Cem. Concr. Res. 34 (2004) 1733–1777.
[20] S.Y. Hong, F.P. Glasser, Alkali sorption by CSH and CASH gels: Part II. Role of alumina, Cem. Concr. Res. 32 (2002) 1101–1111.
[21] E. L'Hôpital, B. Lothenbach, G. Le Saout, D. Kulik, K. Scrivener, Incorporation of aluminium in calcium-silicate-hydrates, Cem. Concr. Res. 75 (2015) 91–103.
[22] E. L'Hôpital, B. Lothenbach, K. Scrivener, D.A. Kulik, Alkali uptake in calcium alumina silicate hydrate (CASH), Cem. Concr. Res. 85 (2016) 122–136.
[23] M.D. Jackson, S.R. Chae, S.R. Mulcahy, C. Meral, R. Taylor, P. Li, A.-H. Emwas, J. Moon, S. Yoon, G. Vola, H.R. Wenk, P.J.M. Monteiro, Unlocking the secrets of Al-tobermorite in roman seawater concrete, Am. Mineral. 98 (2013) 1669–1687.
[24] M.D. Jackson, S.R. Mulcahy, H. Chen, Y. Li, Q. Li, P. Cappelletti, H.R. Wenk, Phillipsite and Al-tobermorite mineral cements produced through low-temperature water-rock reactions in Roman marine concrete, Am. Mineral. 102 (2017) 1435–1450.
[25] J. MacFarlane, T. Vanorio, P.J.M. Monteiro, Multi-scale imaging, strength and permeability measurements: Understanding the durability of Roman marine concrete, Constr. Build. Mater. 272 (22) (2021), 121812.
[26] L. Casson, Ships and Seamanship in the Ancient World, Princeton University Press, Princeton, 1971.
[27] K. Holum, R.L. Hohlfelder, King Herod's Dream: Caesarea on the Sea, Norton, New York, 1988.
[28] A. Raban, Sebastos, the herodian harbour of caesarea: how it was built and operated, Center for Maritime Studies Newsletter 19 (1992) 3–6.
[29] C. Brandon, Cements, Concrete, and Settling Barges at Sebastos: Comparisons with Other Roman Harbor Examples and the Descriptions of Vitruvius, in: A. Raban, K.G. Holum (Eds.), Caesarea Maritima: A Retrospective after Two Millennia, Brill Academic Pub, Leida, 1996, pp. 25–40.
[30] J.P. Oleson, Artifactual Evidence for the History of the Harbors of Caesarea, in: A. Raban, K.G. Holum (Eds.), Caesarea Maritima: A Retrospective after Two Millennia, Brill Academic Pub, Leida, 1996, pp. 359–377.
[31] A. Raban, K. Holum, Caesarea Maritima: A Retrospective after Two Millennia, E.J, Brill, Leiden, 1996.
[32] R.L. Hohlfelder, Beyond coincidence? Marcus agrippa and king herod's harbor, J. Near Eastern Studies 59 (2000) 241–253.
[33] J.I. Boyce, E.G. Reinhardt, A. Raban, M.R. Pozza, Marine Magnetic Survey of a Submerged Roman Harbour, Caesarea Maritima, Israel, Inter. J. Nautical Archaeology 33 (2004) 122–136.
[34] E. Netzer, The Architecture of Herod the Great Builder, Mohr Siebeck, Tubingen, 2006.
[35] E. Reinhardt, B. Goodman, J. Boyce, G. Lopez, P. Hengstum, W. Rink, Y. Mart, A. Raban, The tsunami of 13 December A.D. 115 and the destruction of herod the great's harbor at caesarea maritima, Israel. Geology 34 (2006) 1061–1064.
[36] R.L. Hohlfelder, C. Brandon, J.P. Oleson, Constructing the harbour of caesarea palaestina, israel: new evidence from the ROMACONS Field Campaign of October 2005, Inter. J. Nautical Archaeology 36 (2) (2007) 409–415.
[37] G.F. Votruba, Imported building materials of Sebastos Harbour, Israel, Inter. J. Nautical Archaeology 36 (2) (2007) 325–335.
[38] A. Raban, The Harbour of Sebastos (Caesarea Maritima) in its Roman Mediterranean Context, BAR Publishing, Oxford, 2009.
[39] G. Vola, E. Gotti, C. Brandon, J.P. Oleson, R.L. Hohlfelder, Chemical, mineralogical and petrographic characterization of Roman ancient hydraulic concretes cores from Santa Liberata, Italy, and Caesarea Palestinae, Israel. Periodico di Mineralogia 80 (2) (2011) 317–338.
[40] B.M.D. Bergin, The innovative genius of herod at caesarea maritima, Cultural and Religious Studies 6 (7) (2018) 377–390.
[41] Y. Asscher, A. van Zuiden, C. Elimelech, P. Gendelman, J. Sharvit, M. Secco, G. Ricci, G. Artioli, Prescreening hydraulic lime-binders for disordered calcite in caesarea maritima: Characterizing the chemical environment Using FTIR, Radiocarbon 62 (3) (2020) 527–543.
[42] M. Secco, S. Dilaria, A. Addis, J. Bonetto, G. Artioli, M. Salvadori, The evolution of the Vitruvian recipes over 500 years of floor-making techniques: the case studies of the *Domus delle Bestie Ferite* and the *Domus di Tito Macro* (Aquileia, Italy), Archaeometry 60 (2018) 185–206.
[43] M. Secco, C. Previato, A. Addis, G. Zago, A. Kamsteeg, S. Dilaria, C. Canovaro, G. Artioli, J. Bonetto, Mineralogical clustering of the structural mortars from the Sarno Baths, Pompeii: A tool to interpret construction techniques and relative chronologies, J. Cult. Heritage 40 (2019) 265–273.
[44] S. Dilaria, C. Previato, M. Secco, M.S. Busana, J. Bonetto, J. Cappellato, G. Ricci, G. Artioli, P. Tan, Phasing the history of ancient buildings through PCA on mortars' mineralogical profiles: the example of the Sarno Baths (Pompeii), Archaeometry 64 (4) (2022) 866–882.
[45] H. Rietveld, H.,, A profile refinement method for nuclear and magnetic structures, J. Appl. Crystallogr. 2 (1969) 65–71.
[46] S.I. Tsipursky, V.A. Drits, The distribution of octahedral cations in the 2:1 layers of dioctahedral smectites studied by oblique-texture electron diffraction, Clay Miner. 19 (1984) 177–193.
[47] W. Dollase, Correction of intensities for preferred orientation in powder diffractometry: application of the March model, J. Appl. Crystallogr. 19 (1986) 267–272.
[48] T. Taut, R. Kleeberg, J. Bergmann, The new seifert rietveld program BGMN and its application to quantitative phase analysis, Materials Structure 5 (1) (1998) 55–64.
[49] K. Ufer, G. Roth, R. Kleeberg, H. Stanjek, R. Dohrmann, J. Bergmann, Description of X-ray powder pattern of turbostratically disordered layer structures with a Rietveld compatible approach, Z. Kristallogr. 219 (2004) 519–527.
[50] N. Döbelin, R. Kleeberg, Profex: a graphical user interface for the Rietveld refinement program BGMN, J. Appl. Crystallogr. 48 (2015) 1573–1580.
[51] I.T. Jolliffe, Principal Component Analysis. Springer Series in Statistics, Springer-Verlag, New York, 2002.

[52] A. Addis, M. Secco, F. Marzaioli, G. Artioli, A. Chavarria Arnau, I. Passariello, F. Terrasi, G.P. Brogiolo, Selecting the most reliable ^{14}C dating material inside mortars: the origin of the Padua cathedral, Radiocarbon 61 (2) (2019) 375–393.

[53] D. Massiot, F. Fayon, M. Capron, I. King, S. Le Calvé, B. Alonso, J.O. Durand, B. Bujoli, Z. Gan, G. Hoats, Modelling one- and two-dimensional solid-state NMR spectra, Magn. Reson. Chem. 40 (2002) 70–76.

[54] K.M. Poduska, L. Regev, E. Boaretto, L. Addadi, S. Weiner, L. Kronik, S. Curtarolo, Decoupling local disorder and optical effects in infrared spectra: differentiating between calcites with different origins, Adv. Mater. 23 (4) (2011) 550–554.

[55] L. Regev, K.M. Poduska, L. Addadi, S. Weiner, E. Boaretto, Distinguishing between calcites formed by different mechanisms using infrared spectrometry: archaeological applications, J. Archaeol. Sci. 37 (12) (2010) 3022–3029.

[56] Y. Asscher, G. Dal Sasso, L. Nodari, I. Angelini, T.B. Ballaran, G. Artioli, Differentiating between long and short range disorder in infra-red spectra: on the meaning of "crystallinity" in silica, PCCP 19 (32) (2017) 21783–21790.

[57] T.B. Coplen, Reporting of stable hydrogen, carbon, and oxygen isotopic abundances (technical report), Pure Applied Chemistry 66 (1994) 273–276.

[58] S.T. Kim, T.B. Coplen, J. Horita, Normalization of stable isotope data for carbonate minerals: implementation of IUPAC guidelines, Geochim. Cosmochim. Acta 158 (2015) 276–289.

[59] R.V. Fisher, H.U. Schmincke, Pyroclastic Rocks, Springer-Verlag, Berlin, 1984.

[60] C.K. Wentworth, A scale of grade and class terms for clastic sediments, J. Geol. 30 (5) (1922) 377–392.

[61] R.J. Dunham, Classification of carbonate rocks according to depositional textures, in: W.E. Ham (Ed.), Classification of Carbonate Rocks — A Symposium, AAPG Memoir, 1, Tulsa, Oklahoma, 1962, pp. 108–121.

[62] M.B. Toffolo, The significance of aragonite in the interpretation of the microscopic archaeological record, Geoarchaeology 36 (2021) 149–169.

[63] K.J.D. MacKenzie, M.E. Smith, Multinuclear Solid-State NMR of Inorganic Materials, Pergamon, Oxford, 2002.

[64] J. Brus, S. Abbrent, L. Kobera, M. Urbanova, P. Cuba, Advances in ^{27}Al MAS NMR Studies of Geopolymers, in: G.A. Webb (Ed.), Annual reports in NMR Spectroscopy, 88, Elsevier, Amsterdam, 2016, pp. 79–146.

[65] V.C. Farmer, The infrared spectra of minerals, Mineralogical Society, London, 1974.

[66] A. Fernández-Jiménez, A. Palomo, Mid-infrared spectroscopic studies of alkali-activated fly ash structure, Microporous Mesoporous Mater. 86 (1–3) (2005) 207–214.

[67] P. Rovnaník, P. Bayer, P. Rovnaníková, Characterization of alkali activated slag paste after exposure to high temperatures, Constr. Build. Mater. 47 (2013) 1479–1487.

[68] W. Zhu, X. Chen, L.J. Struble, E.H. Yang, Characterization of calcium-containing phases in alkali-activated municipal solid waste incineration bottom ash binder through chemical extraction and deconvoluted Fourier transform infrared spectra, J. Cleaner Prod. 192 (2018) 782–789.

[69] F. Puertas, M. Palacios, H. Manzano, J.S. Dolado, A. Rico, J. Rodríguez, A model for the CASH gel formed in alkali-activated slag cements, J. Eur. Ceram. Soc. 31 (12) (2011) 2043–2056.

[70] M.B. Toffolo, Radiocarbon Dating of Anthropogenic Carbonates: What Is the Benchmark for Sample Selection? Heritage 3 (4) (2020) 1416–1432.

[71] A. Peccerillo, Plio-Quaternary Volcanism in Italy: Petrology, Geochemistry, Springer, Berlin, 2005.

[72] Colella, A., Di Benedetto, C., Calcaterra, D., Cappelletti, P., D'Amore, M., DI Martire, D., Graziano, S.F., Papa, L., de Gennaro, M., Langella, A., 2017. The Neapolitan Yellow Tuff: An outstanding example of heterogeneity. Construction and Building Materials 136, 361-373.

[73] Lancaster, L., 2012. Ash mortar and vaulting tubes: agricultural production and the building industry in North Africa, in: Camporeale, S., Dessales, H., Pizzo, A. (Eds.), Arqueología de la construcción III. Los procesos constructivos en el mundo romano: la economía de las obras, École Normale Supérieure (Paris, 10-11 Diciembre 2009), Consejo Superior de Investigaciones Científicas, Madrid-Mérida, pp. 145–160.

[74] L. Lancaster, Pozzolans in Mortar in the Roman Empire: An Overview and Thoughts on Future Work, in: I.F. Ortega, S. Bouffier (Eds.), Mortiers et hydraulique en Méditerranée antique, Archéologies Méditerranéennes 6, Presses Universitaires de Provence, Aix-en-Provence, 2019, pp. 31–39.

[75] M.J. Kohn, Carbon isotope compositions of terrestrial C3 plants as indicators of (paleo)ecology and (paleo)climate, Proc. Natl. Acad. Sci. 107 (46) (2010) 19691–19695.

[76] M.H. O'Leary, Carbon isotopes in photosynthesis, Bioscience 38 (5) (1988) 328–336.

[77] S. Eggels, S. Blankenagel, C.C. Schön, V. Avramova, The carbon isotopic signature of C4 crops and its applicability in breeding for climate resilience, Theor. Appl. Genet. 134 (2021) 1663–1675.

[78] J.C. Vogel, A. Fuls, A. Danin, Geographical and environmental distribution of C3 and C4 grasses in the sinai, negev, and judean deserts, Oecologia 70 (2) (1986) 258–265.

[79] A.F. Diefendorf, K.E. Mueller, S.L. Wing, P.L. Koch, K.H. Freeman, Global patterns in leaf 13 C discrimination and implications for the studies of past and future climate, Proc. Natl. Acad. Sci. 107 (13) (2010) 5738–5743.

[80] A. Avinash, A. Murugesan, Chemometric analysis of cow dung ash as an adsorbent for purifying biodiesel from waste cooking oil, Sci. Rep. 7 (2017) 9526.

[81] Ö. Cizer, K. Van Balen, D. Van Gemert, Competition between hydration and carbonation in hydraulic lime and lime-pozzolana mortars, Adv. Mater. Research 133–134 (2010) 241–246.

[82] B. Kosednar-Legenstein, M. Dietzel, A. Leis, K. Stingl, Stable carbon and oxygen isotope investigation in historical lime mortar and plaster – Results from field and experimental study, Appl. Geochem. 23 (2008) 2425–2437.

[83] G. Ricci, M. Secco, A. Addis, A. Pistilli, N. Preto, G.P. Brogiolo, A. Chavarria Arnau, F. Marzaioli, I. Passariello, F. Terrasi, G. Artioli, Integrated multi-analytical screening approach for reliable radiocarbon dating of ancient mortars, Sci. Rep. 12 (2022) 3339.

[84] P. Colomber, A.R. Grimmer, H. Zanni, P. Sozzani, Nuclear Magnetic Resonance Spectroscopy of Cement-Based Materials, Springer, Berlin, 1998.

[85] A. Alberti, E. Galli, The Structure of Nekoite, $Ca_3Si_6O_{15}•7H_2O$; a New Type of Sheet Silicate, Am. Mineral. 65 (1980) 1270–1276.

[86] S. Merlino, Okenite, $Ca_{10}Si_{18}O_{46}•18H_2O$: The first example of a chain and sheet silicate, Am. Mineral. 68 (1983) 614–622.

[87] K. Garbev, L. Black, G. Beuchle, P. Stemmermann, Inorganic polymers in cement based materials, Wasser- und Geotechnologie 2 (2002) 19–30.

[88] G. Artioli, M. Secco, A. Addis, M. Bellotto, Role of hydrotalcite-type layered double hydroxides in delayed pozzolanic reactions and their bearing on mortar dating, in: H. Pöllmann (Ed.), Cementitious Materials: Composition, Properties, Application, de Gruyter, Berlin, 2017, pp. 147–158.

[89] G. Kovalchuk, A. Fernández-Jiménez, A. Palomo, Alkali-activated fly ash: effect of thermal curing conditions on mechanical and microstructural development–Part II, Fuel 86 (3) (2007) 315–322.

[90] P. Yu, R.J. Kirkpatrick, B. Poe, P.F. McMillan, X. Cong, Structure of calcium silicate hydrate (C-S-H): Near-, Mid-, and Far-infrared spectroscopy, J. Am. Ceram. Soc. 82 (3) (1999) 742–748.

[91] A. Forster, Hot-lime Mortars: A current perspective, J. Architectural Conservation 10 (3) (2004) 7–27.

[92] A. Moropoulou, T. Tsiourva, K. Bisbikou, G. Biscontin, A. Bakolas, E. Zendri, Hot lime technology imparting high strength to historic mortars, Constr. Build. Mater. 10 (2) (1996) 151–159.

[93] Y. Elakneswaran, T. Nawa, K. Kurumisawa, Electrokinetic potential of hydrated cement in relation to adsorption of chlorides, Cem. Concr. Res. 39 (2011) 340–344.

[94] J. Duchesne, E.J. Reardon, Measurement and prediction of portlandite solubility in alkali solutions, Cem. Concr. Res. 25 (5) (1995) 1043–1053.

[95] T.H. Soukissian, D. Denaxa, F. Karathanasi, A. Prospathopoulos, K. Sarantakos, A. Iona, K. Georgantas, S. Mavrakos, Marine renewable energy in the Mediterranean Sea: status and perspectives, Energies 10 (2017) 1512.

[96] M. Secco, L. Maritan, C. Mazzoli, G.I. Lampronti, F. Zorzi, L. Nodari, U. Russo, S. Pesavento Mattioli, Alteration processes of pottery in lagoon-like environments, Archaeometry 53 (4) (2011) 809–829.

[97] R. Hedderich, O. Klimmek, A. Kröger, R. Dirmeier, M. Keller, K.O. Stetter, Anaerobic respiration with elemental sulfur and with disulfides, FEMS Microbiol. Rev. 22 (1999) 353–381.

[98] L.K. Davidson, T. Demeril, R.L. Handy, Soil pulverization and lime migration in soil lime stabilization, Highway Res. Rec. 92 (1965) 103–126.

[99] M.E. Karim, M.J. Alam, M.S. Hoque, Effect of salinity of water in lime-fly ash treated sand, Int. J. Geo-Eng. 8 (2017) 15.

[100] G.W. Brindley, Order-disorder in clay mineral structures, in: G.W. Brindley, D. Brown (Eds.), Crystal Structures of Clay Minerals and Their X-Ray Identification, Mineralogical Society, London, 1980, pp. 125–196.

[101] D.R.M. Brew, F.P. Glasser, Synthesis and characterization of magnesium silicate hydrate gels, Cem. Concr. Res. 35 (1) (2005) 85–98.

[102] G. Ponce-Anton, M.C. Zuluaga, L.A. Ortega, J.A. Mauleon, Petrographic and chemical-mineralogical characterization of mortars from the cistern at amaiur castle (Navarre, Spain), Minerals 10 (4) (2020) 311.

[103] C. Roosz, S. Grangeon, P. Blanc, V. Montouillout, B. Lothenbach, P. Henocq, E. Giffaut, P. Vieillard, S. Gaboreau, Crystal structure of magnesium silicate hydrates (MSH): the relation with 2:1 Mg–Si phyllosilicates, Cem. Concr. Res. 73 (2015) 228–237.

[104] A.G. Dickson, C. Goyet, Handbook of methods for the analysis of the various parameters of the carbon dioxide system in sea water, Oak Ridge National Lab, Oak Ridge, 1994.

[105] T. Katayama, The so-called alkali-carbonate reaction (ACR) – Its mineralogical and geochemical details, with special reference to ASR, Cem. Concr. Res. 40 (4) (2010) 643–675.

[106] M. Boon, W.D.A. Rickard, A.L. Rohl, F. Jones, Stabilization of aragonite: role of Mg^{2+} and other impurity ions, Cryst. Growth Des. 20 (2020) 5006–5017.

[107] J. Grant, G.L. Pesce, R.J. Ball, M. Molinari, S.C. Parker, An experimental and computational study to resolve the composition of dolomitic lime, RCS Advances 6 (2016) 16066–16072.

[108] C. Vasconcelos, J.A. McKenzie, S. Bernasconi, D. Grujic, A.J. Tiens, Microbial mediation as a possible mechanism for natural dolomite formation at low temperatures, Nature 377 (1995) 220–222.

[109] L.M. Seymour, N. Tamura, M.D. Jackson, A. Masic, Reactive binder and aggregate interfacial zones in the mortar of Tomb of Caecilia Metella concrete, 1C BCE, Rome, J. Am. Ceram. Soc. 105 (2) (2022) 1503–1518.